

www.acsami.org Research Article

Characterizing Grain Boundary Effects on Mg²⁺ Conduction in Metal—Organic Frameworks

Yang Wang,[‡] Tongtong Luo,[‡] Brooke Elander, Yu Mu, Dunwei Wang,* Udayan Mohanty,* and Junwei Lucas Bao*



Cite This: ACS Appl. Mater. Interfaces 2023, 15, 21659-21678



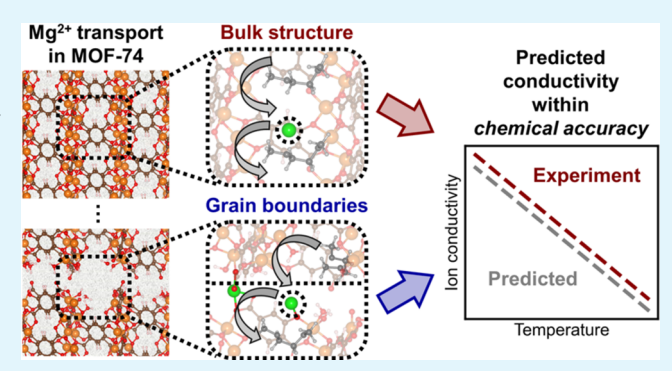
ACCESS I

III Metrics & More

Article Recommendations

s Supporting Information

ABSTRACT: Next-generation materials for fast ion conduction have the potential to revolutionize battery technology. Metalorganic frameworks (MOFs) are promising candidates for achieving this goal. Given their structural diversity, the design of efficient MOF-based conductors can be accelerated by a detailed understanding and accurate prediction of ion conductivity. However, the polycrystalline nature of solid-state materials requires consideration of grain boundary effects, which is complicated by challenges in characterizing grain boundary structures and simulating ensemble transport processes. To address this, we have developed an approach for modeling ion transport at grain boundaries and predicting their contribution to conductivity. Mg²⁺ conduction in the Mg-MOF-74 thin film was studied as a



representative system. Using computational techniques and guided by experiments, we investigated the structural details of MOF grain boundary interfaces to determine accessible Mg²⁺ transport pathways. Computed transport kinetics were input into a simplified MOF nanocrystal model, which combines ion transport in the bulk structure and at grain boundaries. The model predicts Mg²⁺ conductivity in the MOF-74 film within chemical accuracy (<1 kcal/mol activation energy difference), validating our approach. Physically, Mg²⁺ conduction in MOF-74 is inhibited by strong Mg²⁺ binding at grain boundaries, such that only a small fraction of grain boundary alignments allow for fast Mg²⁺ transport. This results in a 2–3 order-of-magnitude reduction in conductivity, illustrating the critical impact of the grain boundary contribution. Overall, our work provides a computation-aided platform for molecular-level understanding of grain boundary effects and quantitative prediction of ion conductivity. Combined with experimental measurements, it can serve as a synergistic tool for characterizing the grain boundary composition of MOF-based conductors.

KEYWORDS: metal-organic framework,, Mg-MOF-74, grain boundary, interface structure,, ion conductivity, kinetic modeling, ion transport mechanism

1. INTRODUCTION

Solid-state materials for ion conduction have the potential to transform current battery technology. Among these, metal—organic frameworks (MOFs) show promise due to their large structural diversity and amenability to chemical functionalization. For MOF-based ion conductors, accurate understanding and prediction of conductivity can greatly facilitate the rational design of transport properties. However, due to the polycrystal-line nature of solid-state materials, grain boundaries have major effects on ion conduction processes, which are not well understood. Thus, to enhance chemical insight and accelerate material screening, we have developed a synergistic approach for molecular-level characterization and quantitative prediction of ion transport at grain boundaries. In addition, this can be used to determine the grain boundary composition of solid-state materials such as MOFs.

Previous work has demonstrated the utility of MOF as a solidstate material for ion conduction. Porous MOFs, such as those based on MOF-74,³ have shown relatively high conductivities for monovalent and divalent cations.^{4–7} The addition of negatively charged functional groups to MOF can enable additional enhancements in ion transport,^{8–10} with decent conductivity achieved for even trivalent cation species.⁵ These ion-conductive properties of MOF have been exploited in the development of battery systems.^{11,12} MOF can be utilized as an anodic anion trap to enhance Li⁺ transference number in Li-

Received: February 17, 2023 Accepted: April 7, 2023 Published: April 21, 2023





based batteries, improving cycling stability and energy efficiency. ¹³ UiO-66 and its functionalized derivatives have been explored as potential anode materials for potassium-ion batteries. ^{14,15} MOF as a selective separator for the suppression of unwanted species in binary-electrolyte batteries has also been demonstrated. ^{16,17} These studies show the viability of ion-conducting MOF and its application to battery technology. Given the diversity of MOF structures and their large potential for functionalization, a systematic approach to understanding and predicting ion transport properties can accelerate the further development of MOF-based ion conductors.

However, accurate understanding and quantitative prediction of ion conductivity require consideration of polycrystalline grain boundary effects. This is highlighted by the important role of grain boundaries in a wide range of solid-state materials. For instance, Li⁺ transport in perovskite is significantly inhibited by the defect composition and orientation of the perovskite grain boundary. ^{18–22} Na⁺ conductivity of NASICON is slightly slowed by grain boundaries, though to a lesser extent than perovskites. 23,24 Cation conduction in other oxide materials has also been studied, generally showing an inhibitory influence from grain boundaries. For instance, grain boundaries in the Li₇La₃Zr₂O₁₂ pellet reduce its Li⁺ conductivity by multiple orders of magnitude.²⁹ On the other hand, reducing grain boundary size via yttrium-doping can enhance lithiation processes in ${\rm Li_8ZrO_6}$. Various mechanisms by which boundary effects can impact ion transport have been proposed, including structural distortions at the grain boundary, charge carrier depletion, and formation of a secondary phase.³¹ These findings illustrate the importance of understanding and accounting for the grain boundary contribution to ion conductivity.

Although past studies of MOF have revealed grain boundary effects for a wide range of applications, the specific impact on ion conduction remains poorly understood. One example is defect density in UiO-66,32 which has been shown to regulate the catalytic activity of deposited Cu nanoparticles. 33,34 In addition, proton conduction in MOF can be improved by increasing the MOF grain particle size and reducing grain boundary density.³⁵ Recent work has also been done in the orientation and alignment control of nanocrystals during MOF synthesis. 36,37 Finally, Hou, et al. show that regulating the orientation of MOF grain boundaries can dramatically improve the efficiency of gasphase hydrocarbon separations.³⁸ In contrast, less progress has been made in characterizing grain boundary effects on ion transport and acquiring a molecular-level understanding of transport processes. This is in spite of the potential significance of MOF-based ion conductors and is partly due to challenges arising from the structural complexity of MOF systems. These challenges include a more intricate molecular structure at the grain boundary and the problem of combining different grain boundary interfaces to obtain ensemble transport properties.

To address these issues, we have developed an approach for understanding and predicting grain boundary contributions to ion conductivity in MOF-based materials. Combined with experimental conductivity measurements, this approach can be applied to quantitatively characterize the grain boundary composition of solid-state ion conductors. Mg²⁺ conduction in the Mg-MOF-74³ thin film was studied as a representative system.^{39–43} Mg²⁺-based electrochemistry is a potential strategy for overcoming the limitations of lithium-ion batteries.⁴⁴ However, Mg²⁺ exhibits lower mobility in the solid state ^{45,46} and poor intercalation properties with conventional cathodes,⁴⁷ and these shortcomings can be addressed by MOF.^{17,48} MOF-

74 is one of the first MOFs investigated for its ion-conductive properties. Cation conduction in MOF-74 has been studied under various electrolyte compositions. A,6 Room-temperature ion conductivities of up to 10⁻⁴ S/cm have been achieved, indicating the potential for battery applications. The powder form of MOF-74 is most extensively studied, while recent work has reported on its thin-film synthesis. Promisingly, the MOF-74 film has the potential to act as a selective separator in binary-electrolyte battery designs. The high density of open metal sites (OMSs) can trap anion and solvent species, suppressing the transport of unwanted electrolytes while enabling cation conduction. T,48 This represents a key motivation for using MOF-74 as the representative system.

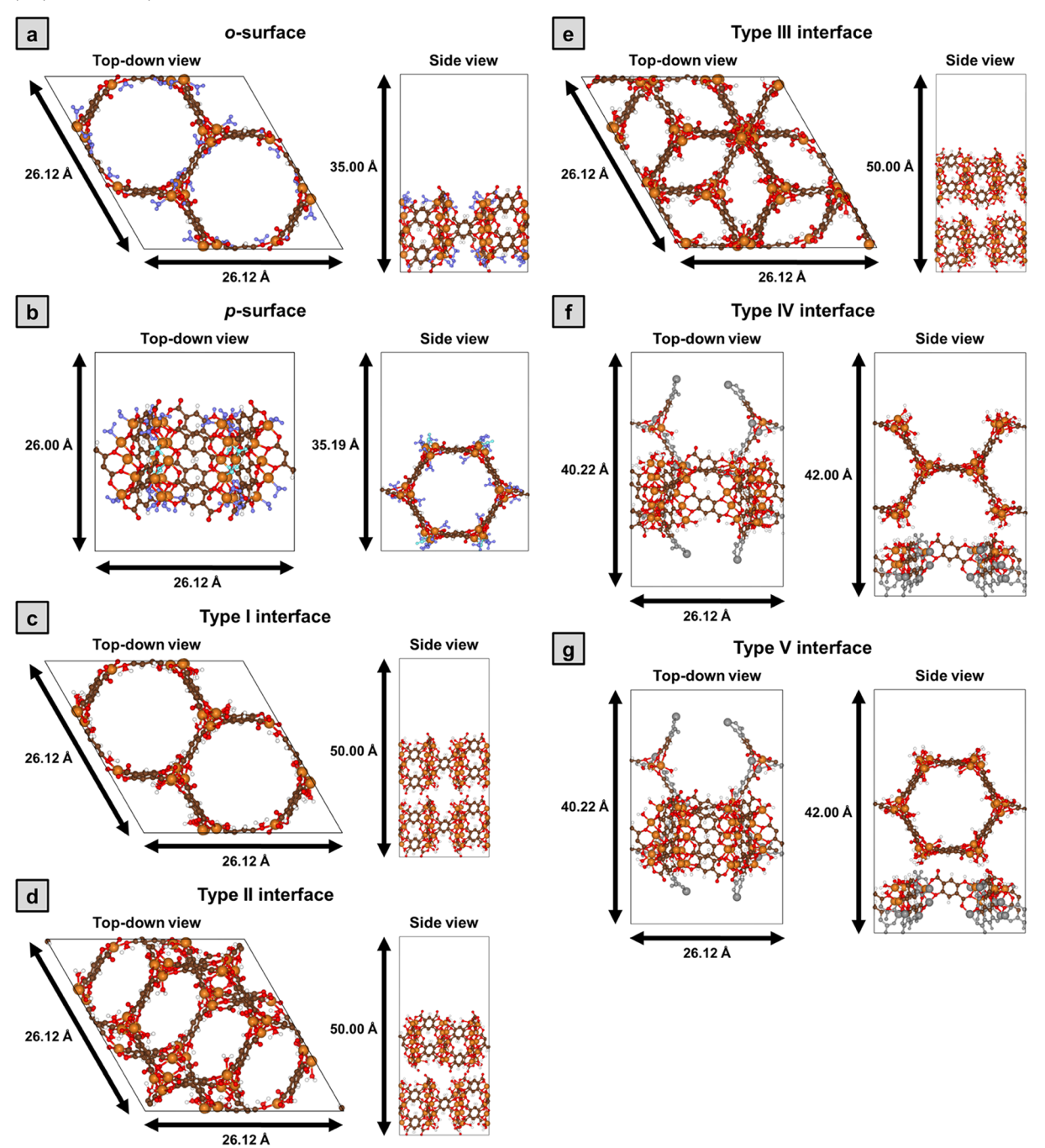
In the current study, we proposed prototypical structures for different surfaces and grain boundary interfaces of the MOF-74 nanocrystal, guided by X-ray diffraction (XRD) data. Kohn—Sham (KS) density functional theory (DFT) was then used to compute mechanisms and energy barriers associated with Mg²⁺ transport at each nanocrystal interface. With these results, we applied kinetic modeling to develop an ion transport model of the MOF nanocrystal, incorporating Mg²⁺ conduction both in the bulk structure and at grain boundaries. We used this model to predict the temperature-dependent Mg²⁺ conductivity of the MOF-74 thin film. The predicted apparent activation energy for Mg²⁺ conduction shows excellent agreement with the experimentally measured value (i.e., within the chemical accuracy threshold of <1 kcal/mol), demonstrating the reliability of our methods.

We find that Mg²⁺ transport in MOF-74 is significantly inhibited at grain boundaries by strong interactions with the MOF organic linker. Only specific alignments of the grain boundary interface preclude linker interactions and allow for ion conduction comparable to that in the bulk structure. The result is that Mg²⁺ conductivity occurs through a small fraction (~0.1%) of ion conduction channels composed of MOF nanocrystals with perfectly aligned grain boundaries. Overall, Mg^{2+} conductivity is reduced by 2-3 orders of magnitude due to the grain boundary contribution, showing the importance of accounting for grain boundary effects. Our approach employs molecular-level modeling of grain boundaries to understand ion transport kinetics and applies this knowledge to quantitatively predict conductivity, which enables accurate screening for efficient MOF-based ion conductors. Combining computation and experiment, it can synergistically characterize grain boundary composition and understand its role in modulating ion transport.

2. COMPUTATIONAL METHODS AND MODELS

2.1. Plane-Wave Density Functional Theory. Plane-wave (PW) DFT calculations in a periodic unit cell (refer to Section 2.2 for cell parameters) were performed with the Quantum Espresso package (version 6.6). We used the Perdew–Burke–Ernzerhof (PBE) exchange–correlation (XC) functional, coupled with Grimme's D2 correction for dispersion interactions. The effect of core electrons was represented by ultrasoft pseudopotentials (USPP). The wavefunction and charge density kinetic energy cutoffs were set to 50 and 500 Ry, respectively. Integration of the Brillouin zone was performed at the γ point. The self-consistent field (SCF) convergence threshold was set to 1×10^{-4} Ry. For structure optimization, the convergence thresholds for total energy and force were set to 1×10^{-4} Ry and 1×10^{-3} Ry/Bohr, respectively, unless otherwise noted. Systems containing one and two Mg²⁺ ions were assigned net charges of +2 and +4, respectively. A neutralizing background charge was applied for periodic charged systems.

Scheme 1. Optimized Structural Models for (a) o- and (b) p-Surfaces (o = Orthogonal, p = Parallel) of the Mg-MOF-74 Nanocrystal, with Associated Lattice Parameters. H₂O and OH⁻ Molecules Used to Cap Unsaturated Mg Metal Nodes at the Surface are Shown in Blue and Teal, Respectively. OH⁻ is Required for the p-Surface to Maintain Charge Balance. Top-Down Perspective Corresponds to Viewing the xy-Plane. Side Perspective Corresponds to Viewing the xz-Plane. (c-g) Optimized Structural Models for Type I, II, III, IV, and V Interfaces with Associated Lattice Parameters. Type IV and V Interface Structures are Partly Truncated, with Atoms near the Truncation Sites Position Restrained (Gray). Atom Color Codes: Orange, Mg; Red, O; Brown, C; and White, H.



2.2. Structural Models. *2.2.1. Bulk Mg-MOF-74.* A $1 \times 1 \times 2$ supercell of Mg-MOF-74 in its conventional unit cell representation was used to model bulk MOF (Figure S1). A supercell is required because Mg²⁺ transport between adjacent binding sites in MOF corresponds to movement from one MOF unit cell to the next. The supercell consists of 324 atoms, and its optimal lattice parameters (a = 26.12 Å, b = 26.12 Å, c = 13.86 Å, $\alpha = 90.0^{\circ}$, $\beta = 90.0^{\circ}$, and $\gamma = 120.0^{\circ}$) were found through variable-cell relaxation. For this relaxation, the kinetic and charge density cutoffs were increased by a factor of 1.2 to

correct for Pulay stress. Afterward, an additional round of fixed-cell relaxation was performed with the optimized lattice parameters held constant.

2.2.2. MOF Nanocrystal Surfaces. We constructed various structural models of the Mg-MOF-74 nanocrystal surface. To construct the surfaces, we truncated the periodic structure of bulk MOF at metallinker bonds. This is consistent with the experimental synthesis of Mg-MOF-74, which involves controlling the formation of metal—organic bonds between Mg metal nodes and 2,5-dihydroxyterephthalate linkers.

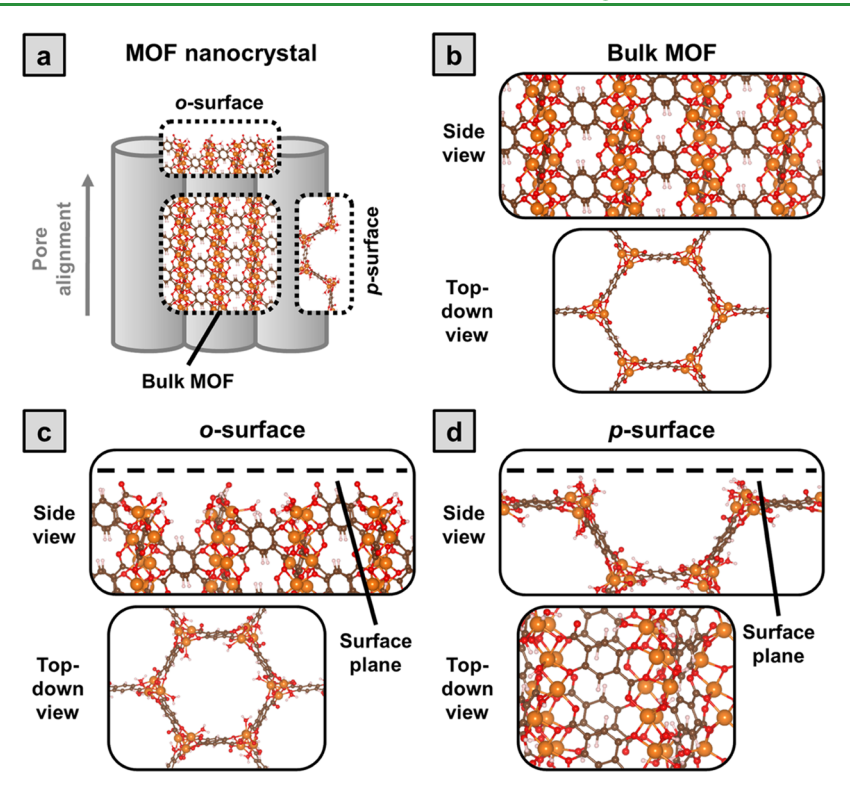


Figure 1. (a) Single MOF nanocrystal is composed of multiple parallel pores, which are cylindrical in geometry, and represented as gray cylinders in the diagram. The number of cylinders is not indicative of the pore number. "Pore alignment" indicates the direction of the pore cylinder axis. The interior of the nanocrystal can be modeled by the bulk structure of MOF-74. The *o*-surface is the surface formed from the termination of the ends of the pore cylinders. The *p*-surface is formed by cutting through the body of the pore cylinder. (b) Structure of bulk MOF in the interior of the nanocrystal. (c) The structure of the *o*-surface (*o* = orthogonal) of the nanocrystal, where the surface plane is orthogonal to the long axis of the MOF pore cylinder. (d) The structure of the *p*-surface (*p* = parallel), where the surface plane is parallel to the long axis of the pore cylinder. Atom color codes: orange, Mg; red, O; brown, C; and white, H.

Thus, we expect the surface of synthesized MOF nanocrystals to be composed of terminated metal-linker bonds. Exposed metal nodes at the surface are capped with a combination of $\rm H_2O$ and $\rm OH^-$ molecules (Scheme 1a,b), with $\rm OH^-$ used to maintain charge balance. Using this procedure, two representative nanocrystal surfaces, the $\it o-$ and $\it p-$ surfaces, were constructed.

In the *o*-surface (o = orthogonal), the plane of the MOF nanocrystal surface is orthogonal to the MOF-74 pore cylinder. The structure of a single *o*-surface, composed of 342 atoms, is shown in Scheme 1a and Figure 1b. This structure is periodic in the x- and y-directions, while a >20 Å vacuum layer is applied in the z-direction to mitigate the unphysical interaction between periodic images. This results in the following lattice parameters: a = 26.12 Å, b = 26.12 Å, c = 35.00 Å, α = 90.0°, β = 90.0°, and γ = 120.0°.

In the *p*-surface (p = parallel), the plane of the MOF nanocrystal surface is parallel to the MOF pore cylinder. The structure of the *p*-surface is shown in Scheme 1b and Figure 1c. This surface is composed of alternating convex and concave half-pores parallel to the surface plane, which corresponds to truncated pore cylinders. The surface structure is periodic in only the *x*-direction, with a >10 Å vacuum layer applied in the *y*-direction and a >15 Å layer in the *z*-direction. It is composed of 322 atoms and has lattice parameters a = 26.12 Å, b = 26.00 Å, c = 35.19 Å, α = 90.0°, β = 90.0°, and γ = 90.0°.

Fixed-cell structure relaxation was performed on both *o*- and *p*-surfaces to obtain their lowest-energy geometries.

2.2.3. MOF Surface—Surface Interfaces. Next, five different types of interfaces between MOF nanocrystal surfaces were constructed by combining the *o*- and *p*-surfaces.

Type I, II, and III interfaces were formed by stacking together two layers of the *o*-surface along the *z*-direction (Scheme 1c,d,e and Figure 2b). These three interface types differ only in the alignment of the MOF-74 pores on each side of the interface (Scheme 1c,d,e and Figure 2b). The resulting system is composed of 684 atoms and has lattice

parameters a=26.12 Å, b=26.12 Å, c=50.00 Å, $\alpha=90.0^\circ$, $\beta=90.0^\circ$, and $\gamma=120.0^\circ$. A >20 Å vacuum layer is applied in the z-direction. The separation between the two sides of the interface (defined to correspond to the z-direction distance between the two closest atoms on each side of the interface) is initially set to 1 Å. Following fixed-cell relaxation, in which all atoms on each side of the interface are allowed to move, this separation decreases for all three interface types. Because interactions between the surfaces of MOF nanocrystals are more transient and disordered than those constituting the bulk MOF structure, we used a less stringent convergence threshold when optimizing the interface structure. Specifically, we set the total energy and force thresholds to be 2×10^{-4} Ry and 2×10^{-3} Ry/Bohr, respectively.

Type IV and V interfaces were formed by stacking together one layer of the o-surface with one layer of the p-surface along the z-direction (Scheme 1f,g and Figure 2c). Again, the two interface types differ only with respect to alignment between the interface sides (Scheme 1f,g and Figure 1c). In order to accommodate the unit cell of the p-surface structure, the o-surface is transformed into a supercell with 468 atoms and lattice parameters $a = 26.12 \text{ Å}, b = 40.22 \text{ Å}, c = 35.00 \text{ Å}, \alpha = 90.0^{\circ}, \beta$ = 90.0°, and γ = 90.0°. Stacking together the σ -surface supercell with the p-surface results in a combined system having the following lattice parameters: a = 26.12 Å, b = 40.22 Å, c = 50.00 Å, $\alpha = 90.0^{\circ}$, $\beta = 90.0^{\circ}$, and $\gamma = 90.0^{\circ}$. The structure is partially truncated such that it contains 572 atoms in the computational cell. Vacuum layers (>10 Å) are applied in the y- and z-directions. The separation between the interface sides is initially set such that the z-direction distance between the two closest atoms on the two sides is 1 Å. This separation is then optimized through structure relaxation. Once more, we set the total energy and force thresholds to be 2×10^{-4} Ry and 2×10^{-3} Ry/Bohr, respectively, to account for the more transient nature of the surface-surface interactions between MOF nanocrystals.

2.3. Transition States. Minimum-energy pathways (MEP) and energy barriers were calculated using the climbing image nudged elastic band (CI-NEB) method.⁵³ The spring constant connecting the series of images was set to 0.2 Ry/Bohr². A force convergence threshold of $2 \times$ 10⁻³ Ry/Bohr for forces was used. The reaction coordinate of each image is given by

$$s(n) = \sum_{j=2}^{n} \sqrt{\sum_{i=1}^{K} \left[(x_{i,j} - x_{i,j-1})^2 + (y_{i,j} - y_{i,j-1})^2 + (z_{i,j} - z_{i,j-1})^2 \right]}$$
(1

where s(n) is the coordinate of the nth image, K is the number of atoms in the system, and $(x_{i,j}, y_{i,j}, z_{i,j})$ is the Cartesian coordinate of the *i*th atom in the jth image.

The dynamics of Mg²⁺ interface transport is largely confined to the interior of the MOF interface structures. Thus, it is unnecessary to represent the upper and lower ends of the interface, which are >7 Å from where Mg²⁺ transport occurs. Accordingly, to expedite CI-NEB calculations, we reduced the size of the optimized interface structures by further truncating their upper and lower ends at metal-linker bonds (Figures S2 and S3). In addition, position restraints were applied to MOF atoms close to the truncation sites in order to maintain their optimized geometries after truncation. For Type I/II/III interfaces, the reduced system (Figure S2) is composed of 396 atoms and has lattice parameters a = 26.12 Å, b = 26.12 Å, c = 40.00 Å, $\alpha = 90.0^{\circ}$, $\beta = 90.0^{\circ}$, and $\gamma = 120.0^{\circ}$. For the Type IV interface, the reduced system (Figure S3a) is composed of 442 atoms and has lattice parameters a = 26.12 Å, b = 26.12 Å= 40.22 Å, c = 35.00 Å, $\alpha = 90.0^{\circ}$, $\beta = 90.0^{\circ}$, and $\gamma = 90.0^{\circ}$. For the Type V interface, the reduced system (Figure S3b) is composed of 382 atoms with the same lattice parameters as the Type IV interface.

2.4. Energetic Refinement. To obtain more accurate energetics, we used a three-level strategy to refine the single-point energies calculated at the PW-PBE-D2 level.

2.4.1. Electronic Energy. First, we applied a correction to the electronic energy. For this, carved cluster models were constructed based on optimized geometries obtained from periodic PW-PBE-D2 calculations and used without further relaxation (Figure S4). To improve accuracy, energies in the carved cluster were recalculated at the M06-2X/cc-pVTZ level of theory.⁵⁴ We chose the M06-2X hybrid functional because it can predict noncovalent interaction energies and reaction barriers for main group elements with high accuracy. 55,56 Carved cluster calculations were performed using the Gaussian package (version 16.C01). The electronic energy corrected to the M06-2X level, $E_{\text{M06-2X}}$, is given by

$$E_{\rm M06-2X} = E_{\rm PBE-D2}^{\rm PW} + \left(E_{\rm M06-2X/cc\text{-}pVTZ}^{\rm cluster} - E_{\rm PBE-D2/cc\text{-}pVTZ}^{\rm cluster}\right) \tag{2}$$

where $E^{\rm PW}_{\rm PBE-D2}$ is the electronic energy at the PW-PBE-D2 level for the same-level optimized geometry, $E^{\rm cluster}_{\rm M06-2X/cc-pVTZ}$ is the energy at the M06-2X/cc-pVTZ level for the carved cluster, and $E_{\rm PBE-D2/cc-pVTZ}^{\rm cluster}$ is the energy at the PBE-D2/cc-pVTZ level for the carved cluster.

2.4.2. Free Energy of Solvation. Next, we accounted for the effect of solvent. The free energies of solvation $\Delta G_{\rm S}^{\circ}$ were obtained from singlepoint calculations performed on the gas-phase optimized structures. For implicit solvation models based on electron density, the free energy of solvation is included in the single-point SCF energy obtained from a self-consistent reaction field (SCRF) calculation. (This single-point energy is, in fact, the potential of mean force.) Therefore, $\Delta G_{\rm S}^{\circ}$ for a given structure and a particular choice of solvation model is the difference between the SCRF single-point energy and the gas-phase single-point energy, both computed at the same geometry.

We first calculated the solvation energy in the periodic system using the self-consistent continuum solvation (SCCS) model.⁵⁸ This ensured that solvation effects due to periodic boundary conditions were accounted for. Then, in the carved cluster system (Figure S4), we refined the solvation energy using the universal solvation model based on density (SMD), which is extensively parameterized against experimental free energies of solvation.⁵⁹ SMD provides quantitatively reliable solvation energies. Finally, we corrected the contribution of the SCCS solvation energy in the carved cluster with the polarizable

continuum model (PCM).60 We used PCM for the carved cluster because the SCCS model is not available for atom-centered basis set codes, such as Gaussian. Ideally, one should use the same solvation model in order to take full advantage of error cancellation and correct the energy to the SMD level. Nevertheless, the current approach is a good approximation because the electrostatic component of the SCCS model has been parameterized to reproduce exactly that of PCM. 58,61 In addition, our testing shows that solvated energy barriers for Mg²⁺ transport, estimated from SCCS and PCM, are comparable (Figure S5). Calculations were performed using the atom-centered cc-pVTZ basis set, the same as for electronic refinement.

The standard-state free energy of solvation at the SMD level, $\Delta G_{\text{S;SMD}}^{\circ}$, was obtained by

$$\Delta G_{\text{S;SMD}}^{\circ} = \Delta G_{\text{S;SCCS}}^{\text{PW}} + (\Delta G_{\text{S;SMD}}^{\text{cluster}} - \Delta G_{\text{S;PCM}}^{\text{cluster}}) + \Delta G_{\text{S}}^{* \to \circ}$$
(3)

where $\Delta G_{\text{S:SCCS}}^{\text{PW}}$ is the SCCS free energy of solvation calculated in the periodic system with the PW basis at the PBE-D2 level, $\Delta G_{\text{S;SMD}}^{\text{cluster}}$ is the SMD free energy of solvation computed with the carved cluster model using the atom-centered basis set (cc-pVTZ) at the M06-2X level, and $\Delta G_{S,PCM}^{cluster}$ is the PCM free energy of solvation for the carved cluster at the M06-2X level. We assume that the solute-solvent interaction based on solute electron density is sufficiently similar between PBE-D2 and M06-2X. Thus, $\Delta G_{S:SCCS}^{PW}$ (calculated with PBE-D2) is approximately the SCCS solvation free energy at the M06-2X level, such that $G_{S:SMD}^{\circ}$ is approximately the SMD solvation free energy at the M06-2X level for the whole periodic system. $\Delta G_{\rm S}^{*\to\circ}$ is the Gibbs free energy change for converting from the fixed-concentration solvation free energy (i.e., at 1 $\operatorname{mol} L^{-1}$ in solution and in the gas phase) to the standard-state solvation free energy (i.e., at 1 mol L⁻¹ in solution and 1 bar in the gas phase). $\Delta G_{\rm S}^{*\to\circ}$ = +1.9 kcal mol⁻¹ for solutes at 298 K. Note that for processes in which the number of solutes is conserved, this conversion factor does not affect the overall free energy change.

Solvent parameters were set based on the experimental properties of dimethoxyethane (DME) liquid, the same as in our previous study. Specifically, the dielectric constant was set to 7.2, the refractive index to 1.380, and the bulk surface tension to 23.93 mN/m; hydrogen bond basicity was set to 0.45, a value characteristic of ethers and equal to that of dibutyl ether. The nonelectrostatic contribution to solvation energy was turned off for SCCS and PCM calculations, as SMD provides a more reliable estimate of the nonelectrostatic component for organic solvents.⁵⁹

2.4.3. Refined Energy with Solvation. Combining the M06-2X electronic energy and the free energy of solvation, the refined energy with solvation, $E_{M06-2X|SMD}^{refined}$, for a given structure is

$$E_{\text{M06-2X|SMD}}^{\text{refined}} = E_{\text{M06-2X}} + \Delta G_{\text{S;SMD}}^{\circ}$$
(4)

where $E_{\rm M06-2X}$ and $\Delta G_{\rm S;SMD}^{\circ}$ are obtained from eqs 2 and 3.

2.4.4. Thermal Free Energy. We included the vibrational motion of nuclei in the thermal free energy. Vibrational free energies were calculated using the harmonic-oscillator approximation at the PW-PBE-D2 level with the aid of the Phonopy package (version 2.8.1).62 The Hessian matrix was estimated by finite central difference with a step size of 0.01 Å. The SCF convergence threshold was set to 1×10^{-6} Ry for greater accuracy. For each structure, only a subset of atoms near the reaction center was used (Figure S6). The thermal free energy is estimated by

$$G(T) = E_{\text{M06-2YISMD}}^{\text{refined}} + G_{\text{vib}}(T) \tag{5}$$

where $G_{vib}(T)$ is the temperature-dependent (T) vibrational free energy. $G_{vib}(T)$ at each temperature was obtained from the vibrational density of states (VDOS), calculated on a $36 \times 36 \times 36$ q-point mesh. This beyond- γ -point-only approach (via finite difference for vibrational frequencies) provides higher accuracy and ensures convergence of $G_{\text{vib}}(T)$ with respect to phonon wave vectors.

2.5. Rate Constants. Rate constants associated with Mg²⁺ transport in bulk MOF-74 and at the MOF interfaces are obtained by 63

$$k^{\text{TST}} = \frac{k_{\text{B}}T}{h} \exp\left(-\frac{\Delta G^{\ddagger}}{k_{\text{B}}T}\right) \tag{6}$$

where k^{TST} is the rate constant predicted by transition state theory (TST), $k_{\rm B}$ is Boltzmann's constant, T is temperature, h is Planck's constant, and ΔG^{\ddagger} is the thermal free energy barrier (from eq 5).

Due to solvent friction, the transmission coefficient associated with the rate constant is less than unity. To account for frictional effects from solvent, we apply the adiabatic Kramers' correction to the TST rate constant^{64,65}

$$k/k^{\rm TST} = \sqrt{1 + \left(\frac{\zeta_{\rm coll}}{2\omega_{\rm b}}\right)^2 - \frac{\zeta_{\rm coll}}{2\omega_{\rm b}}} \tag{7}$$

where k is the corrected rate constant, ζ_{coll} is the solvent collision frequency, and $\omega_{\rm b}$ is the barrier-crossing frequency. $\omega_{\rm b}$ is approximated by the absolute value of the imaginary frequency of the transition state (Table S1-4). Approximations introduced in eq 7 include: (1) the collision frequency replaces the time-dependent friction coefficient⁶⁵ and (2) the potential in the barrier region is an inverted parabola, 66 defined by $\omega_{\rm b}$.

The collision frequency $\zeta_{\rm coll}$ is estimated assuming hard-sphere collisions between Mg²⁺ and DME solvent

$$\zeta_{\text{coll}} = n\sigma_{\text{coll}} \sqrt{\frac{8k_{\text{B}}T}{\pi\mu}} \tag{8}$$

where n is the number density of solvent molecules, $\sigma_{\rm coll}$ is the collision cross-section, and μ is the reduced mass. $\sigma_{\rm coll}$ is obtained from the sum of the van der Waals radii of the colliding species. Based on our previous study, 48 the van der Waals radius of Mg $^{2+}$ was set to 0.74 Å, while that of DME was calculated from the radii of its functional groups (5.65 Å). The number density n is equal to the liquid density of DME (0.868 g mL⁻¹). From these values, ζ_{coll} was found to be 4.279 THz.

Complementary to the TST-based methods presented here, recent work^{67,68} has applied ab initio molecular dynamics (AIMD) to model ion transport processes in solid materials. However, reliable AIMD simulations require significant statistical sampling of transport events, without which the uncertainty in estimated conductivities is high. This suggests that AIMD is less feasible for studying Mg²⁺ conduction in MOF due to larger structural models (300-500 atoms) and slower rates of transport (Sections 4.3 and 4.4) that limit sampling (especially at room temperature). Moreover, AIMD cannot afford higher-level electronic-structure methods, which can prohibit hybrid-functional and solvation corrections to the electronic energy (Section 2.4). Accordingly, for the current work, we have chosen the TST approach of using rate constants of ion transport to estimate conductivity.

2.6. Kinetic Monte Carlo. Rate constants k associated with Mg^{2+} transport in MOF-74 were calculated using the above procedure (Table S1-4). They were then input into a kinetic model of the MOF nanocrystal. The kinetic model consists of multiple nanocrystal layers, representing sequential hopping sites along the MOF pore cylinders. Refer to Section 4.5.2 for a complete definition of the model. Solving the set of rate equations associated with the kinetic model gives the equilibrium Mg²⁺ concentrations in each layer of the nanocrystal. These concentrations were then used to compute Mg²⁺ conductivity in MOF.

The kinetic Monte Carlo (KMC) method of Gillespie 69 was used to solve the rate equations of the kinetic model. Simulations were performed using the StochKit2 70 package, with GillesPy (version 2) 71 as the programming interface. For each simulation, 10 independent time series were generated, and their ensemble average was taken. The simulation time was set to 100 μ s, at which point the Mg²⁺ number in each nanocrystal layer was well-converged (Figure S7). We used the final 20 μ s of the ensemble time series to estimate the equilibrium number of Mg²⁺ in each layer of the MOF nanocrystal.

From the definition of the nanocrystal kinetic model (Section 4.5.2), the volume occupied by each nanocrystal layer is the same. Moreover, the total volume of all layers is equal to the volume of the MOF nanocrystal. Accordingly, the Mg²⁺ number in each nanocrystal layer is converted to concentration by

$$c_{\text{layer}} = n_{\text{layer}} \frac{c_{\text{nanocrystal}}}{n_{\text{nanocrystal}}}$$
(9)

where c_{layer} is the concentration of Mg²⁺ in a given nanocrystal layer, n_{layer} is the Mg²⁺ number in the layer, $c_{\text{nanocrystal}}$ is the average Mg² concentration in the nanocrystal, and $n_{\text{nanocrystal}}$ is the total Mg²⁺ number in the nanocrystal. Note that values of n_{layer} are computed from rate constants of the kinetic model, which are temperature-dependent. c_{nanocrystal} is approximated by the average Mg²⁺ concentration in Mg-MOF-74. This concentration was previously measured to be 0.13 M for MOF-74 in powder form after solvent exchange and vacuum activation (at 373 K). 48 For the current work, we used the concentration in MOF powder as an estimate of Mg²⁺ concentration in the MOF thin film. Finally, $n_{\text{nanocrystal}}$ was set to 4,300 for all simulated temperatures based on the average Mg²⁺ concentration and the known dimensions of the MOF nanocrystal (refer to Section 4.5.2).

2.7. Conductivity of Nanocrystal Layers. The Mg²⁺ conductivity in each layer of the MOF nanocrystal model is obtained through the Nernst-Einstein relation

$$\sigma = \frac{l^2}{2} k \frac{z^2 F^2}{RT} c \tag{10}$$

where l denotes the hopping distance of Mg^{2+} in the nanocrystal layer, kis the corrected rate constant (eq 7), z is the net charge of Mg^{2+} , F is Faraday's constant, R is the gas constant, and c is the Mg²⁺ concentration of the layer.

For bulk MOF, *l* was set to 6.9 Å, corresponding to the distance between metal nodes along the MOF pore. For Type I, II, and III interfaces, l was set to 8.9, 8.9, and 8.7 Å, respectively. These values correspond to the interface separation, defined as the z-direction distance between the two closest geometrically identical Mg metal nodes on the two sides of the interface (refer to Section 4.2.3).

2.8. MOF Nanocrystal Conductivity. Finally, the total conductivity of a MOF nanocrystal with its interface is calculated by treating its nanocrystal layers as resistors arranged in series. Based on the definition of the nanocrystal model (Section 4.5.2), the conducting cross-sectional area is the same for all layers. Thus, the nanocrystal conductivity is given by:

$$\sigma_{\text{nanocrystal}} = \frac{\sum_{i}^{N} l_{\text{bulk}, i} + l_{\text{interface, } i}}{\sum_{i}^{N} \frac{l_{\text{bulk}, i}}{\sigma_{\text{bulk, } i}} + \frac{l_{\text{interface, } i}}{\sigma_{\text{interface, } i}}}$$
(11)

where $l_{\mathrm{bulk},i}$ and $l_{\mathrm{interface},i}$ are the lengths of the bulk and interface layers, respectively, $\sigma_{\text{bulk},i}$ and $\sigma_{\text{interface},i}$ are their conductivities, and N is the number of bulk layers in the MOF nanocrystal. Again, $l_{\text{bulk},i}$ was set to 6.9 Å, while $l_{\text{interface},i}$ was set to 8.9, 8.9, and 8.7 Å for Type I, II, and III interfaces, respectively.

3. EXPERIMENTAL METHODS

3.1. MOF Synthesis. *3.1.1. Thin-Film Synthesis.* The synthesis of the MOF-74 thin film was modified from our previously reported procedure 17 and chracterized by XRD. Forty milligrams (0.2 mmol) of 2,5-dihydroxyterephthalic acid was dissolved in 5.5 mL of DMF and 5.5 mL of ethanol with 57.2 μ L (1 mmol) of acetic acid. Then, 456 mg (1.8 mmol) of Mg(NO₃)₂·6H₂O was dissolved in 3.6 mL of H₂O. The two solutions were mixed, followed by dropwise addition of 1.9 mL (1.44 mmol) of 0.763 M NaOH aqueous solution. Then, 2.5 mL of this precursor solution was mixed with a 4 mL of dilution solution (1:1:1 DMF/ethanol/water). Fifty microliters of the mixture solution was transferred onto a substrate held in a 35 mL autoclave. At the same time, a 4 mL of vapor source (1:1:1 DMF/ethanol/water) was added to the autoclave. The whole autoclave was then placed in a preheated oven at 373 K for 24 h. After crystallization, DMF and methanol were added to soak the sample for 3 h. This solvent exchange process was repeated 3— 4 times for each solvent. After the above procedure, the product was dried under vacuum at room temperature. The film was further activated under vacuum at 373 K overnight.

3.1.2. X-ray Diffraction Characterization. The structure of the product was confirmed by XRD (Figure S8), conducted on a Bruker D8

diffractometer with a Cu K-lpha X-ray source (1.54 Å) under 40 kV and 30 mA.

3.2. Conductivity Measurements. The MOF-74 thin film was synthesized on a stainless steel substrate for conductivity measurements. The activated film was soaked in 0.3 M $Mg(TFSI)_2$ (TFSI⁻ = bis(trifluoromethane)sulfonamide) in the DME solution for 3 days. It was then taken out and dried in air at room temperature for 1 h to remove visible electrolyte species. Conductivity measurements were performed in a Swagelok-cell setup. Carbon paper with a 0.76 cm diameter was used on the MOF film top as the current collector (Figure S9a). An alternating current (AC) voltage, with a frequency range from 0.1 Hz to 1 MHz and an amplitude of 25 mV, was applied between the two electrodes. The impedance was then obtained from the Nyquist plot (Figure S9c,d) by equivalent circuit fitting (Figure S9b). Fitted parameters are reported in Table S5. The conductivity was calculated based on the thickness of the MOF film and the diameter of the current collector. The MOF thin-film thickness was obtained by a profilometer (Bruker Dektak XTL) and found to be 200 nm.

3.3. Grain Boundary Analysis. *3.3.1. Nanocrystal Orientation.* XRD data was used to determine the nanocrystal orientation and grain size of MOF-74. Based on the XRD pattern (Figure S8), the orientation index (OI)³⁸ was calculated to determine the relative orientations of the MOF nanocrystal grain. OI was obtained from the intensity ratios of the (110) and (300) diffraction peaks. The OI of MOF powder (1.50) and thin film (1.33) are similar, indicating that the nanocrystal orientation in the thin film is random.

3.3.2. Grain Size. The grain size of the MOF nanocrystal was calculated from the XRD pattern using the Scherrer equation 72

$$L = \frac{K\lambda}{w\cos\theta} \tag{12}$$

where L is the grain size, θ is the diffraction angle, λ is the radiation wavelength, w is the peak width at half-maximum, and K is a factor associated with nanocrystal shape. We set K to 0.89 in our calculations.

The grain size was estimated using the (110) and (300) diffraction peaks. Measurements from three independent samples were averaged to obtain the final size (Table S6).

4. RESULTS AND DISCUSSION

4.1. Mg-MOF-74 System. To study grain boundary effects on ion conduction in MOF, we used Mg²⁺ transport in the Mg-MOF-74 thin film as a representative study platform. The MOF-74 structure consists of one-dimensional hexagonal pores, which allow for the anisotropic transport of ion species along the pore direction. The Mg metal node of Mg-MOF-74 contains a coordinatively unsaturated open metal site (OMS) to which nucleophilic species can bind. For the electrolyte, we chose a system consisting of a magnesium cation (Mg²⁺), a bis-(trifluoromethane)sulfonamide anion (TFSI⁻), and a dimethoxyethane solvent (DME), which has potential applications for magnesium-based batteries. ^{73,74}

4.2. MOF Nanocrystal Grain Boundaries. *4.2.1. Nanocrystal Orientation.* Structural models of the MOF-74 grain boundary were constructed based on experimental orientation analysis and theoretical calculations. In order to construct an appropriate model of the MOF nanocrystal and its grain boundary, we first determined the relative orientations of nanocrystal grains in the MOF-74 thin film. To do this, we compared the orientation index (OI)³⁸ of the MOF thin film and MOF powder. Specifically, OI was calculated from the ratio of (110) and (300) diffraction peaks in the XRD pattern (Figure S8). The OIs of the MOF thin film and powder were found to be 1.33 and 1.50, respectively, showing that the distribution of nanocrystal orientations is similar between the film and powder. Since crystal orientation in powder materials is expected to be highly disordered, this suggests that nanocrystals in the MOF

thin film are also disordered in their structural arrangement. Thus, a broad range of geometric alignments and orientations is accessible for Mg-MOF-74 nanocrystals.

4.2.2. Nanocrystal Surfaces. Because of the disordered nature of nanocrystal orientation in Mg-MOF-74, it is possible for any grain boundary to be aligned with the direction of Mg²⁺ conduction. Accordingly, we must consider Mg²⁺ transport at all potential grain boundaries. In order to construct plausible representations of MOF-74 grain boundaries, we first explored the atomic structure of a single MOF nanocrystal. In particular, we focused on modeling the structure of the nanocrystal surface, from which the MOF grain boundary is composed.

A single MOF-74 nanocrystal is composed of multiple pores, which are hexagonal in shape and cylindrical in geometry (Figure 1a). These pore cylinders are arranged in parallel to each other, and Mg²⁺ conduction occurs along the direction of the cylinder. The interior of the nanocrystal can be modeled by the three-dimensional bulk structure of MOF-74 (Figures 1b and S1). The nanocrystal surface is formed from either (1) termination of the MOF crystal structure along the axis of the pore cylinder (Figure 1c and Scheme 1a) or (2) termination of the crystal structure in the direction perpendicular to the pore cylinder axis (Figure 1d and Scheme 1b). If the crystal structure is terminated along the pore, then the plane of the surface that forms is orthogonal to the pore axis. Accordingly, we refer to this surface as the o-surface (o = orthogonal). Otherwise, the plane of the formed surface is parallel to the pore cylinder axis, and we refer to this surface as the p-surface (p = parallel).

The o-surface corresponds to the cylindrical ends of the MOF-74 pores (Figure 1c and Scheme 1a). Species that are transported through the pores, such as Mg^{2+} , enter and exit the MOF bulk structure through the o-surface. In contrast, the p-surface cuts through the pore cylinder, such that it consists of alternating concave and convex half-pores (Figure 1d and Scheme 1b). In the absence of defects (e.g., missing linkers) on the surface structure, species cannot enter or exit the MOF bulk structure through the p-surface.

Based on the synthetic conditions, we expect the *o*- and *p*-surfaces to be formed from the truncation of the metal-linker bonds in the MOF structure. Specifically, the synthesis of Mg-MOF-74 involves the formation of metal—organic bonds between the Mg metal nodes and 2,5-dihydroxyterephthalate linkers. As a result, the surface structure contains Mg metal nodes that are highly unsaturated with respect to coordination number. For both *o*- and *p*-surfaces, metal nodes with coordination numbers ranging from three to five are present. For comparison, the coordination number of metal nodes in bulk MOF is five.

We calculated the binding energy of H_2O to unsaturated metal nodes at the MOF nanocrystal surface. We find that binding energies at the surface range from -25 to -41 kcal/mol (PBE-D2 level), depending on the metal node coordination number and H_2O binding geometry (Figure S10). These values are greater than that observed for H_2O (-15 kcal/mol)⁴⁰ and DME binding (-25 kcal/mol)⁴⁸ to metal nodes in the bulk MOF structure. This suggests that small nucleophilic molecules, such as H_2O and DME, are bound to the nanocrystal surface at experimental temperatures (290 to 330 K). Accordingly, in our models of the nanocrystal surface, we cap surface metal nodes with H_2O (Scheme 1a). A small number of OH $^-$ is also used on the p-surface to achieve charge balance (Scheme 1b).

4.2.3. Surface-Surface Interfaces. To study grain boundaries inside MOF-74 and their effect on ion transport, we

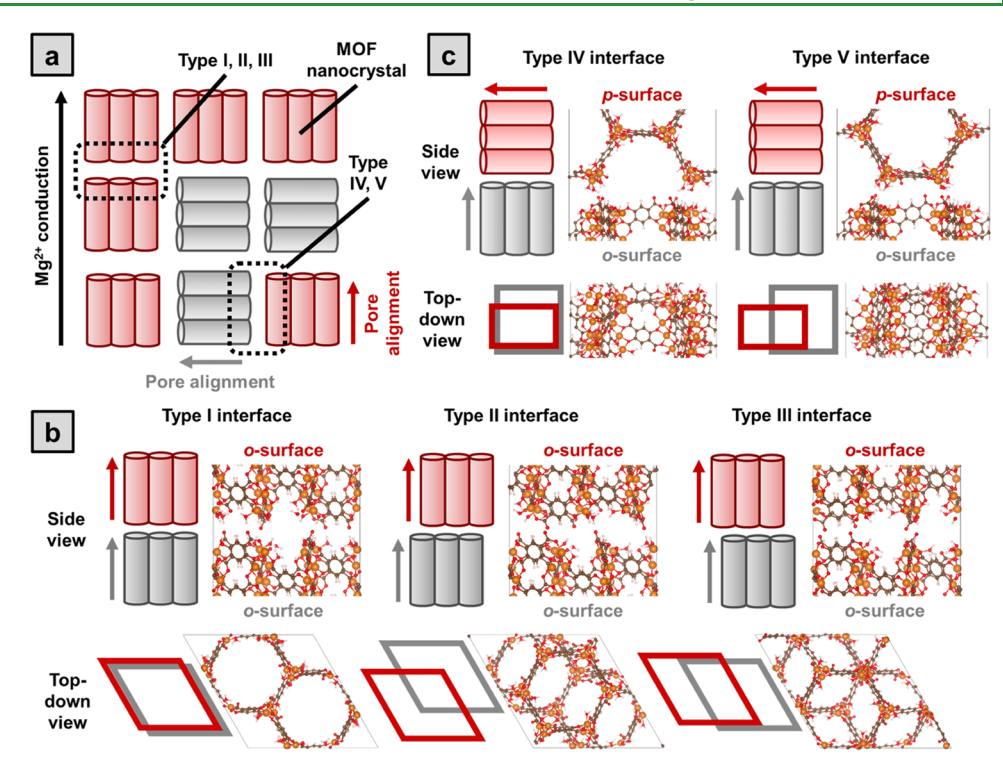


Figure 2. (a) MOF-74 is composed of nanocrystals in a broad range of orientations and alignments. Cylinders represent MOF pores (number of cylinders not indicative of pore number). The disordered arrangement of nanocrystals is supported by XRD data (Figure S8). For a given nanocrystal, the pore cylinder can be oriented in the same direction as Mg²⁺ conduction or in a different direction relative to Mg²⁺ conduction. For Type I, II, and III interfaces, both sides of the interface have pores aligned in the direction of Mg²⁺ transport, while the other side has pores aligned in the perpendicular direction. (b) Type I, II, and III interfaces are constructed from two *o*-surfaces. Mg²⁺ transport can occur across this interface since Mg²⁺ can exit the nanocrystal interior on one side, move through the interface, and enter the nanocrystal interior on the other side. The three interface types differ with respect to the relative alignments of their hexagonal pores. In the Type I interface, the pores on each side of the interface are perfectly aligned; in the Type II interface, the pore hexagons are offset in the direction of the hexagon edge; in the Type III interface, they are offset in the direction of the hexagon vertex. Parallelograms show the alignment of the surface unit cells from the top-down view. (c) Type IV and V interfaces are constructed from a *p*-surface on one side and an *o*-surface on the other. Mg²⁺ transport does not occur across this interface since Mg²⁺ cannot enter or exit through the *p*-surface. Instead, transport occurs in the plane of the interface. Type IV and V interfaces differ with respect to the relative alignments of the interface sides. Rectangles show the alignment of the surface unit cells from the top-down view. Atom color codes: orange, Mg; red, O; brown, C; and white, H.

constructed prototypical interfaces between MOF nanocrystals. Because of the disordered arrangement of nanocrystals in MOF-74, a complete survey requires consideration of interfaces with different alignments and orientations. Thus, we investigated five different types of interfaces (Figure 2). These interfaces are composed of the *o*- and *p*-surfaces described in Section 4.2.2.

Type I, II, and III interfaces are constructed from two osurfaces in contact with each other (Figure 2b; Scheme 1c,d,e). The MOF pore cylinders of one nanocrystal are in parallel with those of the other. Moreover, Mg²⁺ transport can occur across this interface since Mg²⁺ enters and exits the MOF nanocrystal bulk through the o-surface. Type I, II, and III interfaces differ with respect to the alignment of the MOF hexagonal pore between the two sides of the interface. Specifically, Type I represents an interface in which the hexagonal pores on both sides are perfectly aligned relative to each other (Figure 2b, left panel; Scheme 1c). Type II corresponds to an interface in which the pores are offset in the direction of the hexagon edge (Figure 2b, middle panel; Scheme 1d). Type III interfaces are ones in which the offset is in the direction of the hexagon vertex (Figure 2b, right panel; Scheme 1e). Given the geometrical considerations, these three types can be considered representative alignments.

Type IV and V interfaces are constructed from one σ -surface and one p-surface (Figure 2c; Scheme 1f,g). The MOF pore

cylinders of one nanocrystal are perpendicular to those of the other. $\rm Mg^{2+}$ transport does not occur across this interface since species cannot enter or exit the MOF structure through the *p*-surface. Instead, $\rm Mg^{2+}$ transport is expected to occur along this interface (i.e., parallel to the plane of the interface). Specifically, $\rm Mg^{2+}$ conduction can occur along the concave and convex halfpores composing the *p*-surface (Figures 1d and 2c), whose structures are similar to the pore cylinders inside bulk MOF (Figure 1b). Type IV and V interfaces differ in the alignment of the *p*-surface half-pore with respect to the *o*-surface (Figure 2c).

We compared the thermodynamic stability of Type I, II, and III interfaces. After optimizing the structure of each interface, we found the Type I interface to have the lowest energy, while Type II and III interfaces were similar in energy. Specifically, the relative electronic energy per surface area of Type I, II, and III interfaces are 0 (reference), 8.3, and 9.5 kcal $\mathrm{mol}^{-1}~\mathrm{Å}^{-2}$, respectively (PBE-D2 level). This is rationalized by the fact that in the perfectly aligned case of the Type I interface, interactions along the edges of the MOF hexagonal pores are maximized between the two interface sides. In contrast to the interaction energies, the optimized spatial separation between interface sides is approximately the same for all three types (8.9, 8.9, and 8.7 Å for Type I, II, and III interfaces, respectively). This separation is measured by the *z*-direction distance between the two closest geometrically identical Mg metal nodes on the two

sides of the interface. The interface separations are greater than that found between metal nodes in bulk MOF (6.9 Å).

4.3. Mg²⁺ Transport in Bulk MOF. We first investigated Mg²⁺ transport in the interior of a MOF nanocrystal, which is represented by the Mg-MOF-74 bulk structure. Mg²⁺ transport in bulk MOF can occur by three potential mechanisms: (1) diffusion of solvated Mg²⁺ through the MOF pore; (2) hopping of desolvated Mg²⁺ between binding sites on the MOF linker; and (3) hopping of desolvated Mg²⁺ between DME solvent molecules bound to MOF. We calculated energy barriers for each to find the kinetically most accessible mechanism.

To analyze the accessibility of the diffusion mechanism, we compared the dimensions of solvated Mg²⁺ with that of the MOF-74 pore. Although solvated Mg²⁺ is small enough to fit inside an empty MOF pore, it is too large to move through the pore if the OMSs of MOFs are occupied by DME solvent molecules (Figure 3a). This implies that solvated Mg²⁺ diffusion requires a concomitant displacement of DME solvent molecules bound to OMSs. Thus, the diffusion barrier is greater than or equal to the energy barrier for displacing DME from its binding site. We calculated the energy barrier for displacing the DME solvent to be 21 kcal/mol (PBE-D2 level) (Figures 3b and S11), indicating a relatively large barrier for the diffusion mechanism.

Next, we considered hopping mechanisms for desolvated Mg²⁺. These mechanisms are consistent with Grotthuss-like pathways for ion transport, previously observed in MOF and other solid-state conductors. For Mg-MOF-74, two hopping mechanisms are possible depending on the Mg²⁺ binding site, linker hopping and solvent hopping. In linker hopping, Mg²⁺ moves between carboxylate binding sites on the MOF linker (Figure 3c). We calculated the energy barrier for this mechanism to be 25 kcal/mol (PBE-D2) in a previous study.⁴⁸ In solvent hopping, Mg²⁺ moves between ether binding sites on the DME solvent (Figure 3d). These DME solvent molecules are immobilized by binding to the OMSs of MOFs. The energy barrier for this mechanism is 5.6 kcal/mol at the PBE-D2 level, while the refined energy barrier (eq 4) is 5.9 kcal/mol (Figure 3d). This barrier is significantly smaller than the barriers for diffusion and linker hopping mechanisms, indicating that solvent hopping is the dominant mode of Mg²⁺ transport in MOF-74.

Finally, it should be noted that a precondition for the solvent-hopping mechanism is an initial desolvation of Mg^{2^+} . Previous calculations indicate that partial desolvation of $\mathrm{Mg}(\mathrm{DME})_3^{2^+}$, corresponding to the removal of a single DME molecule, is thermodynamically favored in the MOF-74 chemical environment. This is partly due to the interaction of the released DME solvent with OMSs. Thus, most Mg^{2^+} species are partially desolvated when inside MOF, allowing them to engage in the solvent-hopping mechanism. Moreover, the initial desolvation of Mg^{2^+} occurs only once, whereas Mg^{2^+} conduction consists of repeated hops along the full length of the MOF pore. This implies that the contribution of desolvation kinetics to overall ion transport is likely to be negligible.

4.4. Mg²⁺ Transport at MOF Grain Boundaries. Next, we explored Mg²⁺ transport at the MOF nanocrystal interface. For each interface type (I, II, III, IV, and V), we determined the minimum-energy pathway (MEP) and computed the energy barrier for Mg²⁺ transport. Based on the previous analysis (Section 4.3), the most accessible mechanism for Mg²⁺ transport is solvent hopping. In light of this, we only consider the solvent-hopping mechanism at the interface. In addition, we consider only the shortest-distance solvent-hopping pathway under the assumption that the shortest-distance pathway corresponds to

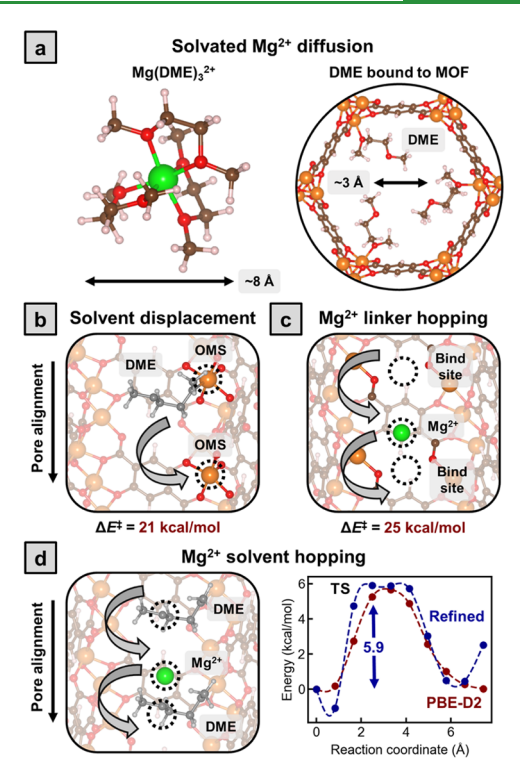


Figure 3. (a) When the DME solvent is bound to Mg-MOF-74, $Mg(DME)_3^{2+}$ is larger than the dimension of the MOF pore with DME (\sim 8 vs \sim 3 Å). Thus, diffusion of solvated Mg²⁺ through MOF-74 can occur only with a concomitant displacement of bound solvent molecules. (b) Displacement of bound DME solvent between open metal sites (OMSs) of Mg-MOF-74. The energy barrier for this process is 21 kcal/mol (PBE-D2 level) (Figure S11), which represents a lower bound for the diffusion barrier of solvated Mg²⁺. (c) In the linker hopping mechanism, Mg²⁺ moves between binding sites on the MOF linker. In particular, the lowest-energy binding site is one where Mg²⁺ is simultaneously bound to two carboxylate groups. The energy barrier for linker hopping was found to be 25 kcal/mol (PBE-D2 level) in a previous study. 48 (d) In the solvent-hopping mechanism, Mg²⁺ moves between binding sites on the DME solvent molecules, which are in turn bound to the OMS of MOF. This process exhibits the lowest energy barrier, at 5.9 kcal/mol (refined level, which includes solvation effects; refer to eq 4). Thus, it is the dominant transport mechanism in bulk MOF. The full minimum-energy pathway (MEP) is shown, with energies reported at both PBE-D2 (red curve) and refined (blue curve) levels. Atom color codes: orange, Mg; red, O; brown, C; white, H; green, Mg²⁺; and gray, DME.

the lowest energy barrier. A justification for this assumption is provided in Section 4.4.3.1. Finally, we show that the calculated Mg²⁺ transport barriers at each interface are also representative of a broad range of interface alignments and orientations.

4.4.1. Type I, II, and III Interfaces. For the Type I interface, where the hexagonal MOF pores are fully aligned across the grain boundary, the Mg²⁺ transport mechanism (Figures 4a and S2a) is similar to that of bulk MOF. The one major difference is that the reaction coordinate length for Mg²⁺ hopping increases from 7 Å in bulk to 11 Å at the Type I interface. As a result of the longer distance, the transport barrier across this interface increases slightly to 7.2 kcal/mol (refined level) for the forward barrier and 6.2 kcal/mol (refined level) for the reverse barrier, compared to bulk MOF (5.9 kcal/mol). Due to structural differences between each side of the interface, the initial and final structures of this transport pathway are not identical. Thus, both forward and reverse processes need to be considered.

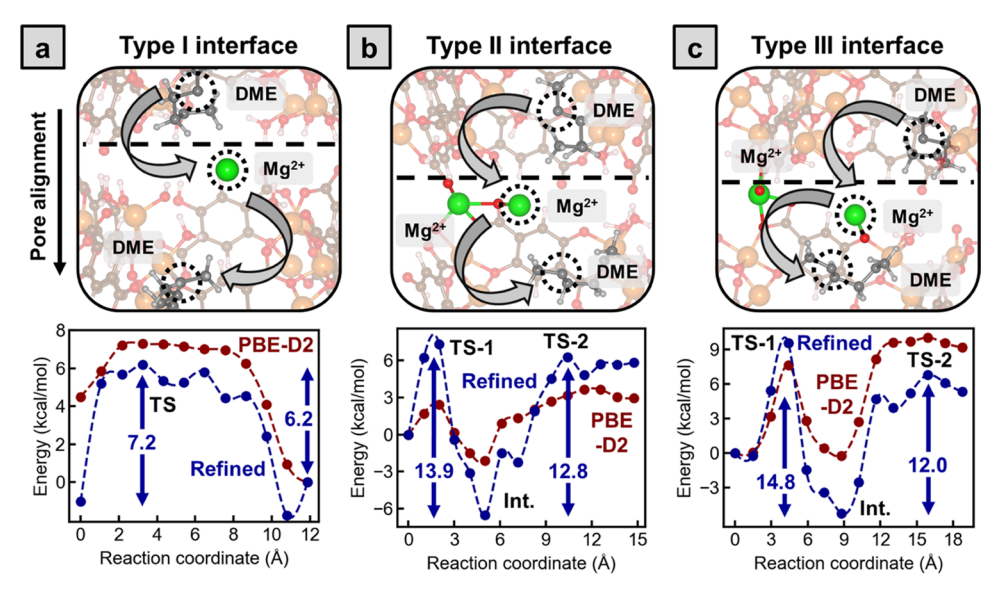


Figure 4. Minimum-energy pathways (MEP) and energy barriers for Mg²⁺ transport across Type I, II, and III interfaces. Dashed lines separate the interface sides. Energies are reported at both the PBE-D2 and refined (eq 4) levels. (a) At the Type I interface, Mg²⁺ transport occurs along the direction of the MOF pore and is similar to the bulk transport mechanism. Solvent hopping occurs between two DME-binding sites on each side of the interface. Due to a greater hopping distance compared to bulk MOF, the energy barrier for transport is slightly higher. Both directions of transport need to be considered since the initial and final structures are not identical. (b) At the Type II interface, Mg²⁺ transport between DME-binding sites is interrupted by interactions with the MOF linker. A binding site proximal to the hopping pathway allows for the interaction of Mg²⁺ with four phenolate/carboxylate groups of the MOF linker. This site is stably occupied by bound Mg²⁺. In the presence of bound Mg²⁺, transport of a free Mg²⁺ also results in binding to a MOF linker carboxylate. This leads to the formation of an intermediate during the transport process. (c) At the Type III interface, a proximal binding site also allows for up to four phenolate/carboxylate interactions with Mg²⁺. This binding site is again stably occupied by bound Mg²⁺. Transport of a free Mg²⁺ leads to binding to a MOF linker phenolate, which is an intermediate in the transport pathway. Atom color codes: orange, Mg; red, O; brown, C; white, H; green, Mg²⁺; and gray, DME.

For the Type II interface, where MOF pores on each interface side are misaligned, the Mg²⁺ transport mechanism is disrupted by Mg²⁺ binding to exposed linker molecules at the interface (Figures 4b and S2b). Specifically, because of the misalignment of the pores, there are multiple linker sites to which Mg²⁺ can bind during transport across the interface. Moreover, these linker sites are highly nucleophilic due to the absence of connecting metal nodes at the MOF nanocrystal surface. We find that in the case of the Type II interface, a strong binding site is located in close proximity to the solvent-hopping pathway. At this binding site, Mg²⁺ can form four metal—oxygen bonds with carboxylate and phenolate groups of the MOF linker (Figure 4b), such that the binding energy is >30 kcal/mol (PBE-D2 level). Due to the high energy of binding, we expect this site to be consistently and stably occupied by an Mg²⁺ ion that does not participate in solvent-hopping transport. In the presence of this bound Mg²⁺, transport of another free Mg²⁺ can still occur. Due to the presence of the bound Mg²⁺, the free Mg²⁺ binds to a less stable site during transport, where it forms only a single Mg²⁺oxygen bond with an exposed carboxylate of the MOF linker. This results in the formation of an intermediate during interface transport, where Mg²⁺ is partly "trapped" by the linker (Figure 4b). Escape from this intermediate requires overcoming an energy barrier of 12.8 kcal/mol (refined level) in the forward direction, which is thermally accessible. Similarly, the energy barrier for reverse transport is 13.9 kcal/mol (refined level). However, these transport barriers are still significantly greater than that for the bulk MOF (5.9 kcal/mol) and the Type I interface (6.2 and 7.2 kcal/mol).

For the Type III interface, Mg²⁺ transport is also disrupted by binding to linker molecules (Figures 4c and S2c). These linker binding sites are proximal to the Mg²⁺ hopping pathway due to

misalignment of the interface sides. Similar to the Type II interface, a strong binding site for Mg^{2+} can be found close to the hopping pathway (Figure 4c). The Mg^{2+} binding energy for this site is again >30 kcal/mol (PBE-D2 level), indicating that it is consistently occupied by an Mg^{2+} ion. In the presence of a bound Mg^{2+} , another free Mg^{2+} can undergo transport via solvent hopping. The free Mg^{2+} also interacts with the MOF linker during transport (although at a less stable site), leading to the formation of an intermediate (Figure 4c). Escape from this intermediate requires 12.0 kcal/mol (refined level) in the forward direction and 14.8 kcal/mol (refined) in the reverse direction.

Although the overall process of Mg²⁺ transport is similar for Type II and III interfaces, there are some notable differences. The Mg²⁺ transport intermediate in the Type II interface forms through binding to a carboxylate group (Figure 4b), while the intermediate in the Type III interface forms through binding to phenolate (Figure 4c). In addition, the bound Mg²⁺ in the Type II interface is more proximal to the intermediate binding site of free Mg²⁺. Specifically, the free Mg²⁺ intermediate is separated from bound Mg²⁺ by only two bonds in the Type II interface (Figure 4b), compared to seven bonds in the Type III interface (Figure 4c).

The analysis of Mg²⁺ transport across Type I, II, and III interfaces shows that alignment of the MOF-74 pore at the grain boundary is key for determining the transport pathway and associated energy barrier. Specifically, grain boundaries with misaligned pores, such as the Type II and III interfaces, produce strong Mg²⁺ interactions with MOF at the grain boundary. As a result, Mg²⁺ becomes partly trapped at the grain boundary, significantly inhibiting its transport through MOF. Only grain boundaries with well-aligned MOF pores, such as the Type I

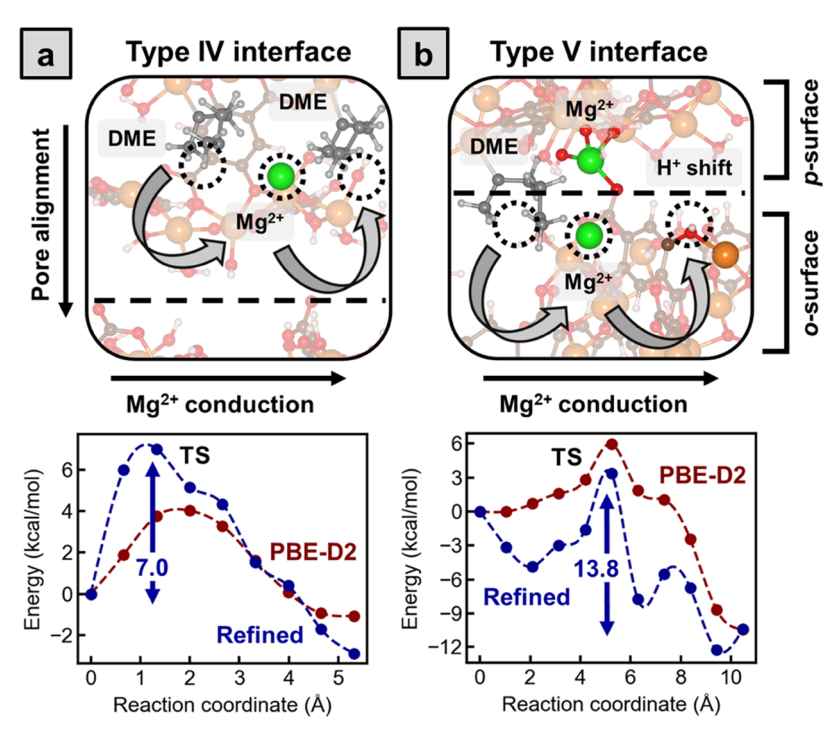


Figure 5. Minimum-energy pathways (MEP) and energy barriers for Mg^{2+} transport along Type IV and V interfaces. Mg^{2+} conduction is parallel to the plane of the interface. Dashed lines separate the interface sides. Energies are reported at both the PBE-D2 and refined (eq 4) levels. (a) At the Type IV interface, Mg^{2+} solvent hopping occurs in the concave half-pore of the *p*-surface. Because the transport pathway is distal to the *o*-surface, hopping is not disrupted. (b) At the Type V interface, Mg^{2+} solvent hopping occurs on the convex half-pore of the *p*-surface. Proximity to the *o*-surface results in Mg^{2+} linker interactions that disrupt solvent hopping. A binding site proximal to the hopping pathway allows for the interaction of Mg^{2+} with phenolate/carboxylate groups of the MOF linker. This site is stably occupied by bound Mg^{2+} . In the presence of bound Mg^{2+} , the transport of a free Mg^{2+} results in binding to a MOF linker phenolate. A proton shift from the phenolate occurs concomitantly with Mg^{2+} binding. Atom color codes: orange, Mg; red, O; brown, C; white, H; green, Mg^{2+} ; and gray, DME.

interface, allow for Mg²⁺ conduction comparable to that in bulk MOF. This suggests that grain boundaries have an overall effect of limiting ion conductivity in MOF.

Finally, we discuss the effects of the energetic refinement approach (eq 4) on the calculated energy barriers. Energetic refinement increases the Mg^{2+} transport barrier, relative to the PBE-D2 level, for Type II and III interfaces while having a lesser impact on the Type I interface (Figure 4). This increase is due to both the M06-2X electronic-structure correction (eq 2) as well as the solvation free energy (eq 3). Intermediate states, in which Mg^{2+} binds directly to the MOF linker, are further stabilized at the M06-2X level, elevating the barrier for escape. In addition, the solvation of Mg^{2+} is less favorable in the transition state than for the intermediate, perhaps due to the confined nature of the MOF pore. Thus, refinement of the energy barriers reinforces the conclusion that Mg^{2+} transport across misaligned grain boundaries is strongly inhibited by interactions with MOF.

4.4.2. Type IV and V Interfaces. For Type IV and V interfaces, Mg²⁺ transport does not occur across the interface since the *p*-surface on one side of the interface prevents entry of Mg²⁺ into the interior of the MOF nanocrystal. Instead, transport occurs parallel to the interface, along the half-pores composing the *p*-surface (Figure 5).

In the case of the Type IV interface, Mg^{2+} transport occurs along the concave half-pores of the *p*-surface (Figures 2c, 5a, and S3a), which are distal to the *o*-surface on the other side of the interface (Figure 2c). As a result, Mg^{2+} solvent hopping is not disrupted by Mg^{2+} -linker interactions with the other side. The energy barrier for transport was found to be 7.0 kcal/mol

(refined), similar to that in bulk MOF (5.9 kcal/mol) and the Type I interface (6.2 and 7.2 kcal/mol) (Figure 5a).

In contrast, for the Type V interface, Mg²⁺ transport occurs along the convex half-pores of the p-surface, which are in close proximity to the other side of the interface (Figures 2c, 5b, and S3b). Because of this, various Mg^{2+} binding sites on the o-surface can disrupt solvent hopping by Mg^{2+} . In particular, a strong binding site in which Mg^{2+} simultaneously binds to four carboxylate/phenolate groups (three on the p-surface and one on the *o*-surface) is observed near the hopping pathway (Figure 5b). Mg²⁺ binds to this site with a binding energy of >30 kcal/ mol (PBE-D2 level), indicating consistent occupation. In the presence of this bound Mg2+, an additional free Mg2+ can undergo solvent hopping. However, the transport of this free Mg²⁺ is also disrupted by interactions with a phenolate group on the o-surface (Figure 5b). In the absence of Mg²⁺ interactions, this phenolate has a proton bound to it. However, when Mg²⁺ interacts with the phenolate, this induces the proton to shift to an adjacent carboxylate group (Figure 5b). The energy barrier required for free Mg²⁺ to escape from phenolate-binding is 13.8 kcal/mol (refined level), which includes the contribution of the concomitant proton shift. This barrier is higher than the transport barrier along the Type IV interface (7.0 kcal/mol) and more in line with that observed for the Type II and III interfaces.

For Type IV and V interfaces, their contribution to the total ion conductivity in MOF is expected to be small relative to Type I, II, and III interfaces. This is because Mg^{2+} transport occurs along these interfaces instead of across them. As a result, the surface area through which Mg^{2+} moves (i.e., the surface area of Mg^{2+} flux) is much smaller in Type IV/V interfaces than in Type

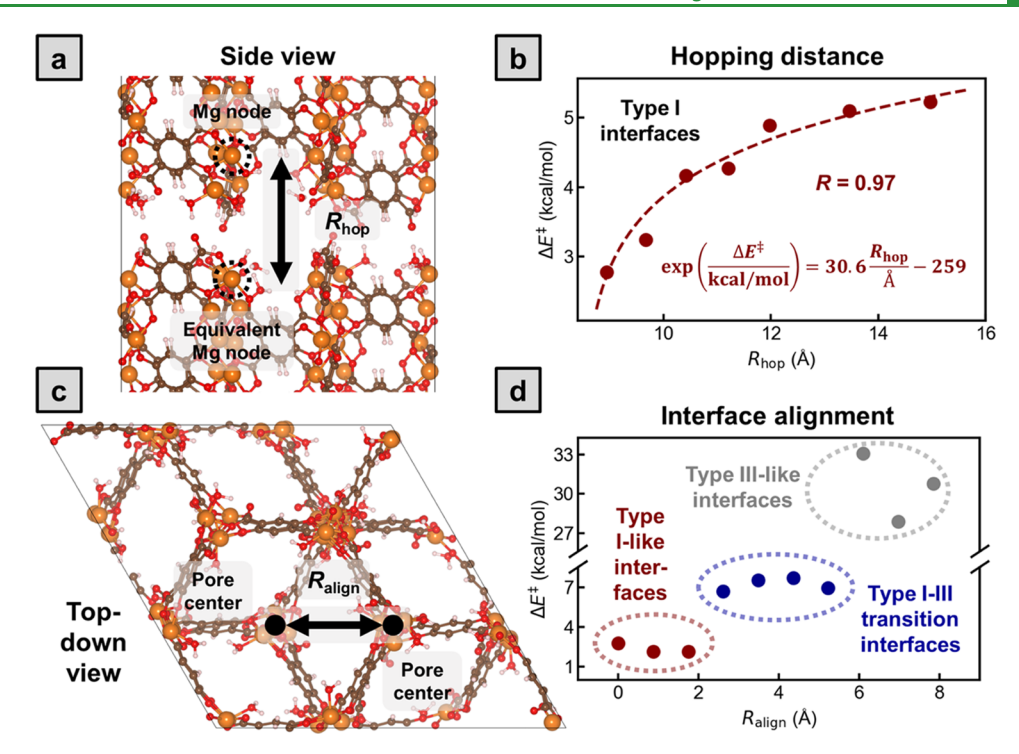


Figure 6. (a) Side view of a Type I interface. R_{hop} is defined as the distance between the two closest geometrically equivalent Mg metal nodes (dashed circle) on each side of the interface; it is a measure of the separation between the interface sides and of Mg²⁺ solvent-hopping distance at the interface. $R_{\text{hop}} = 8.9 \text{ Å}$ in the fully optimized structure of the Type I interface (Figure 4a and Scheme 1c). (b) Energy barrier (ΔE^{\ddagger}) of Mg²⁺ solvent hopping as a function of R_{hop} , calculated at the PBE-D2 level. The data is fit to a logarithmic curve (dashed line) with a correlation coefficient (R_{I}) of 0.97. (c) Topdown view of a Type III interface. R_{align} is the in-plane distance between the centers of the MOF pores on each side of the interface. It is a measure of the relative alignment of the two sides of the interface. For the Type I interface, where MOF pores on each interface side are perfectly aligned, $R_{\text{align}} = 0$; for the Type III interface, where MOF pores are misaligned, $R_{\text{align}} = 8.7 \text{ Å}$; R_{align} in between these values correspond to intermediate alignments between Type I and III interfaces. (d) Energy barrier (ΔE^{\ddagger}) of Mg²⁺ solvent hopping (PBE-D2 level) as R_{align} shifts from Type I to Type III. The change in ΔE^{\ddagger} occurs in discrete jumps, such that three clusters can be identified (red, blue, and gray dashed circles). For R_{align} between 0 and 2 Å (Type I-like, red), no Mg²⁺-linker interactions occur during solvent hopping, resulting in low $\Delta E^{\ddagger} \sim 2-3 \text{ kcal/mol}$; for R_{align} between 2 and 6 Å (Type I-IIII transition, blue), a weak Mg²⁺-linker interaction occurs in the transport pathway, resulting in a small increase to $\Delta E^{\ddagger} \sim 6-8 \text{ kcal/mol}$; for R_{align} between 6 and 8 Å (Type III-like, gray), a much stronger interaction occurs during transport, leading to a large increase to $\Delta E^{\ddagger} \sim 6-8 \text{ kcal/mol}$; for R_{align} between 6 and 8 Å (Type III-like interfaces (gray

I/II/III interfaces. This leads to a reduction in their contribution to total Mg²⁺ conduction. However, the feasibility of Mg²⁺ transport along these interfaces, as demonstrated here, suggests that they can play an important role. In particular, transport along these interfaces allows Mg²⁺ to overcome blockages created by the disordered orientation of nanocrystals (Figure 2a). This is especially true of the Type IV interface, where the Mg²⁺ transport barrier is relatively low and close to that in bulk MOF.

4.4.3. MOF Grain Boundary Ensemble. To characterize Mg²⁺ conduction at the MOF-74 grain boundary, we studied five prototypical interfaces (Type I–V), which were constructed based on the experimentally determined random orientation of MOF nanocrystals. Here, we demonstrate that these interface models are largely representative of the overall ensemble of transport pathways at the grain boundary. To do this, we investigate the effect of (1) Mg²⁺ hopping distance and (2) alignment of the interface sides on the Mg²⁺ transport barrier.

4.4.3.1. Hopping Distance across Grain Boundaries. In computing the Mg²⁺ solvent-hopping barrier across each interface type, we considered only the shortest-distance hop across the interface. This was done under the assumption that the shortest-distance hopping pathway generally corresponds to the pathway with the lowest energy barrier. To justify this assumption, we investigated the effect of hopping distance on

the Mg^{2+} hopping barrier. For this, we used the Type I interface model and increased the separation of the two sides of the interface (Figures 6a and S12a-c). This increase in separation can be measured with the hopping coordinate R_{hop} , defined as the distance between the two closest Mg metal nodes that are geometrically equivalent on each side of the interface (Figure 6a).

The Mg²⁺ transport barrier (PBE-D2 level) was calculated at each separation distance and was found to increase monotonically with R_{hop} (Figures 6b and S13). Specifically, the transport barrier correlates with R_{hop} quantitatively, i.e., $\Delta E^{\ddagger}/(\text{kcal mol}^{-1}) \propto \ln(R_{\text{hop}}/\text{Å})$, for which the correlation coefficient is 0.97 (Figure 6b). Consequently, the solvent-hopping rate of Mg²⁺ is inversely proportional to the hopping distance (to some power α):

$$r \propto \exp\left(-\frac{\Delta E^{\ddagger}}{RT}\right) \propto \exp\left(-c\frac{\ln R_{\text{hop}}}{RT}\right) = R_{\text{hop}}^{-\alpha}$$
 (13)

where r is the rate of Mg²⁺ solvent hopping, ΔE^{\ddagger} is the hopping barrier, R is the gas constant, T is temperature, and c is a fitting constant (Figure 6b) for the relation between ΔE^{\ddagger} and R_{hop} . α is given by

$$\alpha = \frac{c}{RT} \tag{14}$$

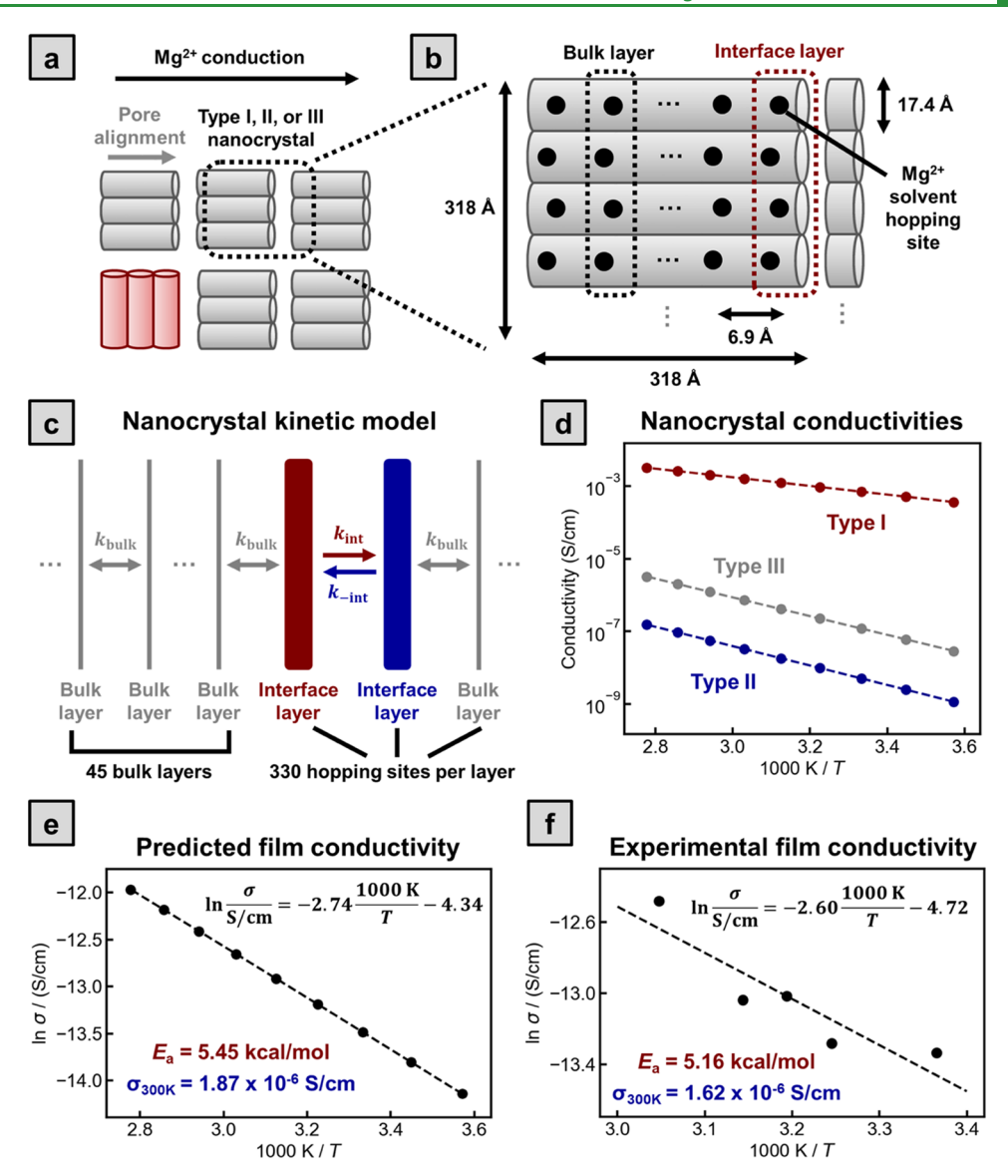


Figure 7. (a) Mg-MOF-74 film is composed of many nanocrystals in different orientations and alignments. A MOF nanocrystal can have either a Type I, II, or III interface with its adjacent nanocrystal. Accordingly, the nanocrystal with its interface (dashed frame) can be classified as Type I, II, or III, depending on the interface type. (b) A single MOF-74 nanocrystal is composed of multiple pore cylinders (gray) arranged in parallel. From XRD data, the average length, width, and height of a nanocrystal is 318 Å (assuming approximate rectilinear geometry). From the MOF-74 crystal structure, the diameter of a single MOF pore is 17.4 Å, while the separation between Mg^{2+} solvent-hopping sites along the pore is 6.9 Å. This implies that there are approximately 330 MOF pores per nanocrystal and around 47 Mg^{2+} hopping sites per MOF pore. The MOF nanocrystal can be subdivided into bulk and interface layers (dashed frames). (c) Kinetic model of a MOF nanocrystal with its interface. The constituting species of the kinetic model are the layers of the nanocrystal. There are 45 bulk layers and two interface layers, with 330 Mg^{2+} hopping sites in each layer. Mg^{2+} transport between bulk layers is governed by k_{bulk} in both directions; transport between interface layers is governed by k_{int} and $k_{\text{-int}}$ for forward and reverse directions, respectively. The kinetic model is periodic, with its leftmost layer connected to its rightmost layer. (d) Temperature-dependent Mg^{2+} conductivity of MOF nanocrystals with Type I, II, and III interfaces. The conductivity of the Type I nanocrystal is orders of magnitude higher than those of Type II and III nanocrystals. (e) Predicted Mg^{2+} conductivity of the MOF-74 thin film. The relative frequency of pure Type I conduction channels is set to 0.2%. The apparent activation energy (E_a) is obtained by fitting ln σ to 1/T. E_a is independent of the relative frequency of Type I channels. σ_{300K} is the conductivity at room temperature. (f

The inverse proportionality between the rate of Mg²⁺ solvent hopping and hopping distance indicates that the shortest hopping pathway is the most accessible. This justifies our approach of using the shortest hopping pathway in calculating the Mg²⁺ transport barrier at the MOF grain boundary. Coincidentally, the relation for Mg²⁺ transport expressed in eq 13, where the shortest hop occurs with the highest probability, is reminiscent of electron transfer behavior in biomolecular systems.⁷⁵

4.4.3.2. Alignment of Grain Boundaries. Next, we determined the effect of alignment between the two sides of the MOF interface on the Mg²⁺ transport barrier. Through this, we can show that the Type I–V interfaces we have considered are representative of a broad range of interface alignments and provide insight into the overall ensemble of MOF grain boundaries. In particular, we studied the set of interface alignments that are intermediate between the alignments observed in Type I and III interfaces (Figures 6c and S12d—

f). This set of alignments can be characterized by the coordinate $R_{\rm align}$, which measures the xy in-plane distance between the MOF pore centers on each side of the interface (Figure 6c). In the Type I interface, where MOF pores on the interface sides are perfectly aligned (Figure 2b, left panel), $R_{\rm align} = 0$. In the Type III interface, where the MOF pore center on one interface side is aligned with the pore vertex on the other side (Figure 2b, right panel), $R_{\rm align} = 8.7$ Å. For interface alignments intermediate between that of Type I and III interfaces, $R_{\rm align}$ is between 0 and 8.7 Å.

For each intermediate interface alignment between Type I and III, we computed the Mg^{2+} transport barrier at the PBE-D2 level (Figures 6d and S14). We found that the energy barrier increases in discrete jumps as interface alignment changes. Specifically, for $R_{\rm align}$ between 0 and 2 Å, where the MOF interface alignment closely resembles that of the Type I interface (Figure S12d), the Mg^{2+} transport barrier is 2–3 kcal/mol (Figures 6d and S14a), which is close to the transport barrier observed at the Type I interface (2.8 kcal/mol at the PBE-D2 level). This is because the Mg^{2+} solvent-hopping mechanism for this set of interface alignments is similar to that of the Type I interface, where Mg^{2+} moves directly across the interface without disruption by MOF linker molecules (Figure S14a). Accordingly, interfaces with this set of alignments can be regarded as "Type I-like interfaces".

For $R_{\rm align}$ between 2 and 6 Å, the MOF interface alignment resembles neither Type I nor Type III but rather the transition between the two (Figure S12e). We refer to interfaces with this set of alignments as "Type I–III transition interfaces". The Mg^{2+} transport barrier across Type I–III transition interfaces is 6–8 kcal/mol (Figures 6d and S14b). This increase in the energy barrier relative to Type I-like interfaces is due to the formation of an intermediate during transport, in which Mg^{2+} binds to a carboxylate of the MOF linker (Figure S14b). However, this binding is relatively weak, as the linker carboxylate also engages in hydrogen bonding with a water molecule.

Finally, for $R_{\rm align}$ between 6 and 8 Å, the MOF interface alignments resemble that of Type III, such that they can be regarded as "Type III-like interfaces". In Type III-like interfaces, Mg^{2+} can engage in binding to an interface-exposed carboxylate of the MOF linker while also bound to the DME solvent (Figure S14c). The strong interaction with the carboxylate leads to a change in energy of 27-34 kcal/mol when Mg^{2+} moves from one side of the interface to the other (Figure 6d). This implies that the Mg^{2+} transport barrier between the two sides of the interface is >27 kcal/mol since the change in energy is a lower bound to the barrier. Thus, Mg^{2+} transport barriers at Type III-like interfaces are significantly greater than those at Type I-like and Type I–III transition interfaces due to stronger Mg^{2+} interactions with the MOF linker.

These results indicate that nanocrystal grain boundaries with qualitatively similar alignments share almost the same Mg²⁺ transport barrier. Specifically, small alignment shifts do not alter the Mg²⁺ transport pathway, so the transport barrier remains the same. Rather, a large, qualitative change in the interface alignment is required to alter the transport pathway and associated energy barrier. This suggests that, in terms of Mg²⁺ transport, a single interface model can represent a broad range of interfaces with similar alignments. Accordingly, we expect the Type I–V interface prototypes surveyed in this work to provide more general insights regarding the ensemble of interface structures and transport pathways at the MOF grain boundary.

4.5. Mg²⁺ Conductivity in MOF. 4.5.1. Nanocrystal Grain Properties. The ion conductivity of MOF-74 thin film was predicted from a simplified model of the MOF nanocrystal and its grain boundary interface. Calculated conductivities were then compared with experimental values, giving insights into the grain boundary composition of MOF. To predict Mg²⁺ conductivity in Mg-MOF-74, we developed a model of the MOF nanocrystal with its grain boundary (Figure 7a,b). Because an accurate model of the nanocrystal requires information regarding its grain size, we first performed experimental characterization of the nanocrystal grain. Specifically, we used eq 12 to calculate the dimensions of the MOF nanocrystal from its XRD pattern.

Based on the XRD data, we find that the average nanocrystal length of Mg-MOF-74 is 318 Å (Figure 7b and Table S6). This length is 6-7 times smaller than the experimentally characterized thickness of the MOF-74 thin film (~200 nm). From the crystal structure of MOF-74, the diameter of the MOF pore cylinder is known to be 17.4 Å (Figure 7b). This implies that a MOF-74 nanocrystal with relatively rectilinear geometry (i.e., 318 Å \times 318 Å \times 318 Å in dimension) has approximately 330 pores. Similarly, based on the nanocrystal dimension, the length of each MOF pore is 318 Å. From the crystal structure, the distance separating sequentially adjacent OMSs along the MOF pore is 6.9 Å (Figure 7b). This implies that each MOF nanocrystal pore contains around 47 sequential OMSs along its axis, to which DME solvent molecules bind. This, in turn, indicates that there are approximately 47 Mg²⁺ solvent-hopping sites sequentially arranged along a single pore of the MOF nanocrystal.

4.5.2. Nanocrystal Kinetic Model. To simulate Mg²⁺ transport through MOF nanocrystals, from which we can calculate the ion conductivity, we develop a kinetic model of the nanocrystal with its grain boundary. Because Mg²⁺ transport occurs in parallel along the direction of the nanocrystal pores, it is convenient to treat the "layers" of the MOF nanocrystal as the constituting species of the kinetic model. Specifically, a nanocrystal layer is a cross-sectional element of the set of parallel pore cylinders composing the MOF nanocrystal (Figure 7b). It is defined to have the following properties:

- (1) The plane of the cross-section encompasses all nanocrystal pores, such that its length and width have the same dimension as the nanocrystal (318 $\text{Å} \times 318 \text{ Å}$).
- (2) The height of the cross-section is such that, for each nanocrystal pore, only a single Mg²⁺ solvent-hopping site is included. Accordingly, the cross-section height is equal to the distance separating sequential hopping sites along the MOF pore (6.9 Å).

In addition, each cross-section can be classified as either a "bulk layer" or an "interface layer", depending on whether it is located in the interior of the MOF nanocrystal or at the grain boundary (Figure 7b).

With a layer defined in this way, the nanocrystal kinetic model is composed of multiple nanocrystal layers arranged in series (Figure 7c). Mg²⁺ transport between sequential bulk layers corresponds to Mg²⁺ solvent hopping inside bulk MOF. Similarly, Mg²⁺ transport between adjacent interface layers corresponds to Mg²⁺ hopping at the MOF interface. Given the dimensions of the MOF nanocrystal, the number of nanocrystal layers in the kinetic model is 47 (refer to Section 4.5.1). Of these, 45 are bulk layers, and two are interface layers (Figure 7c). Moreover, the number of Mg²⁺ solvent-hopping sites in each nanocrystal layer is expected to be 330. Finally, the kinetic model

is periodic, such that its leftmost layer is connected to its rightmost layer.

The rate constants of the kinetic model $(k_{\rm bulk}, k_{\rm int}, {\rm and} \ k_{\rm -int}$ in Figure 7c) are estimated from the energy barriers for Mg²⁺ transport in bulk MOF (Figure 3d) and at Type I/II/III interfaces (Figure 4). Vibrational free energies are added to the refined electronic energy barriers (eq 5) to obtain free energy barriers for Mg²⁺ solvent hopping (Table S1-4). The rate constants are then calculated from the free energy barriers (eqs 6 and 7).

For analysis with the kinetic model, we only consider Mg^{2+} transport across Type I, II, and III interfaces while ignoring Mg^{2+} conduction along Type IV and V interfaces (Figure 5). This is because the contribution of Type IV/V interfaces to the total ion conductivity is nearly negligible, owing to the much smaller surface area of ion flux when Mg^{2+} moves along these interfaces. Specifically, at Type I/II/III interfaces, the number of MOF pores through which Mg^{2+} conduction occurs is around 330, while at Type IV/V interfaces, this number is $\sqrt{330} \cong 18$. This suggests that the contribution to ion conductivity from Type IV/V interfaces is approximately 5% of that from Type I/II/III interfaces.

The number of Mg^{2+} ions in a MOF nanocrystal is determined by the Mg^{2+} concentration in Mg-MOF-74. This concentration has been measured to be 0.13 M in MOF powder, ⁴⁸ and we assume that the value for the MOF film is similar. With a rectilinear MOF nanocrystal (318 Å × 318 Å × 318 Å), Mg^{2+} number in the nanocrystal is calculated to be approximately 4300, which we set to be the number of ions in the kinetic model. Given its size, a single MOF nanocrystal contains around 15,000 Mg^{2+} solvent-hopping sites. This indicates that approximately 30% of all hopping sites in the nanocrystal are occupied by Mg^{2+} ions, consistent with a Grotthuss-like ion transport mechanism.⁷

The nanocrystal kinetic model relies on a few simplifying assumptions that can influence predicted ion conductivity. One assumption is that of rectilinear geometry for MOF nanocrystals. This assumption affects nanocrystal height and, in turn, the number of layers in the nanocrystal model. In particular, it partly determines the ratio of bulk to interface layers, which impacts the relative contribution of these layers to Mg²⁺ conductivity. A second assumption is that a sufficient number of adjacent hopping sites are active in the MOF nanocrystal. This requires that solvent molecules occupy a majority of OMSs in MOF-74, which is reasonable given the high binding energy (>20 kcal/ mol) of DME solvent (Figure 3b). The presence of inactive hopping sites can lead to an overestimation of ion conductivity. A third assumption is that all Mg²⁺ ions in the MOF nanocrystal participate in ion conduction. Based on our study of the nanocrystal interface (Section 4.4.1), it is likely that a small number of Mg²⁺ ions are trapped at the grain boundary and do not take part in solvent-hopping transport. This would lower the effective ion concentration and result in an overestimation of Mg²⁺ conductivity.

4.5.3. Nanocrystal Conductivities. Applying the nanocrystal kinetic model, we calculated Mg^{2+} conductivity through a single MOF-74 nanocrystal with its grain boundary. First, we classified a MOF nanocrystal as either Type I, II, or III depending on its interface (Figure 7a). For each nanocrystal, we constructed its kinetic model by setting $k_{\rm int}$ and $k_{\rm -int}$ (in Figure 7c) to the rate constants for forward and reverse transport across the corresponding interface type (Tables S2–S4). ($k_{\rm bulk}$ is set to the rate constant for Mg^{2+} transport in bulk MOF; refer to Table S1.) Since these rate constants are temperature-dependent, the

nanocrystal kinetic model also varies with temperature. For a given temperature range (280–360 K), we solved for the equilibrium concentrations of Mg²⁺ in each layer of the MOF nanocrystal (Figure S7) using the kinetic Monte Carlo (KMC) method.⁶⁹ With the Mg²⁺ concentration in each layer, as well as the rate constant for Mg²⁺ transport across that layer, we applied the Nernst–Einstein relation (eq 10) to calculate Mg²⁺ conductivity for each layer of the MOF nanocrystal. Finally, the conductivities across all bulk and interface layers were combined by treating the sequence of nanocrystal layers as an inseries resistor (eq 11). This gives the Mg²⁺ conductivity of the MOF nanocrystal (Figure 7d), which is dependent on temperature.

Analyzing the conductivities of each nanocrystal type, we find that MOF nanocrystals with a Type I interface exhibit the highest Mg²⁺ conductivity (Figure 7d). Type III nanocrystals have the second-highest conductivity, and Type II nanocrystals have the lowest. These trends agree with the Mg²⁺ transport barriers at Type I, II, and III interfaces (Figure 4). More specifically, Mg²⁺ conductivity in a nanocrystal with a Type I interface is approximately 3–4 orders of magnitude greater than that with a Type III interface (Figure 7d). Meanwhile, the Type III nanocrystal conductivity is approximately two orders of magnitude greater than that of Type II. Since Mg²⁺ conductivity through Type I nanocrystals is multiple orders of magnitude greater than both Type II and III, ion conduction in MOF-74 occurs overwhelmingly in nanocrystals with Type I interfaces.

In addition to comparing ion conductivities among different nanocrystal types, we also analyzed the relative contribution of the MOF bulk and interface to the total nanocrystal conductivity (Figure S15). For nanocrystals with the Type I interface, we found that bulk and interface conductivities are relatively close, differing by less than one order of magnitude (Figure S15a). As a result, the Mg²⁺ conductivity of the nanocrystal is close to the upper limit of the bulk conductivity. For nanocrystals with Type II and III interfaces, the difference between bulk and interface conductivities is much greater, with Mg²⁺ conductivities at the interface lower by 6-8 orders of magnitude compared to bulk MOF (Figure S15b,c). The effect of the interface significantly reduces the total ion conductivities of Type II/III nanocrystals, such that they are 3–6 orders of magnitude lower than in bulk. The total nanocrystal conductivities are also closer in value to the interface conductivities than to bulk conductivities (Figure S15b,c). These results show that aligned grain boundaries, represented by the Type I interface, dominate Mg²⁺ conductivity in MOF-74, while misaligned grain boundaries, such as Type II and III interfaces, significantly hinder Mg²⁺ transport through the MOF nanocrystal.

Finally, we point out that the nanocrystal kinetic model employed in our calculations (Figure 7c) possesses an asymmetric interface. This is due to the nonequivalence of the forward and reverse rates of $\mathrm{Mg^{2^+}}$ transport at the interface (i.e., k_{int} and $k_{-\mathrm{int}}$). The asymmetry of interface transport is not entirely realistic and originates from the simplified nature of the kinetic model. To correct this, we developed a more detailed kinetic model with a symmetric treatment of the interface (Figure S16a). We find that nanocrystal and MOF film conductivities calculated from the symmetric interface model (Figure S16b,c) are nearly the same as those obtained from the asymmetric-interface model (Figure 7d,e). Thus, although the asymmetric interface in the simplified kinetic model (Figure 7c) is less realistic, it does not noticeably impact model predictions. This justifies the use of the simpler model.

4.5.4. MOF Film Conductivity. The calculated conductivities of Type I, II, and III nanocrystals can further be combined to predict the temperature-dependent Mg²⁺ conductivity of the MOF-74 thin film. The predicted values were then compared with the experimentally measured conductivity to validate our methods.

To calculate the ion conductivity of the MOF-74 film, we modeled the film as consisting of multiple ion conduction channels (Figure S17a). Based on the thickness of the MOF film (~200 nm) and the size of the MOF nanocrystal (318 Å), each conduction channel is composed of around six MOF nanocrystals connected in series (Figure S17a). Adjacent nanocrystals in the conduction channel are separated by grain boundaries with a given alignment (e.g., Type I, II, or III interfaces). The Mg²+ conductivity of the MOF film, $\sigma_{\rm film}$, is given by

$$\sigma_{\text{film}} = \frac{1}{N} \sum_{i}^{N} \sigma_{\text{channel}, i}$$
(15)

where $\sigma_{\text{channel},i}$ is the Mg²⁺ conductivity of the *i*th conduction channel, and *N* is the total number of conduction channels.

Within each conduction channel, the conductivity of Type I nanocrystals (i.e., nanocrystals with Type I-like interfaces) is multiple orders of magnitude greater than that of Type II/III nanocrystals (Figure 7d). Moreover, due to the nature of inseries resistance, the presence of a single Type II/III nanocrystal dramatically reduces the ion conductivity of a conduction channel (Figure S17b). This shows that only ion conduction channels composed purely of Type I nanocrystals contribute significantly to Mg²⁺ conductivity in the MOF film, while the contribution from all other conduction channels is negligible. Accordingly, we ignore conduction channels that are not purely Type I

$$\sigma_{\text{film}} \cong \frac{N_{\text{pure Type I}}}{N} \sigma_{\text{channel}}^{\text{pure Type I}} = \frac{N_{\text{pure Type I}}}{N} \sigma_{\text{nanocrystal}}^{\text{Type I}}$$
(16)

where $\sigma_{\mathrm{channel}}^{\mathrm{pure\ Type\ I}}$ is the Mg²⁺ conductivity of a conduction channel composed purely of Type I nanocrystals and $\frac{N_{\mathrm{pure\ Type\ I}}}{N}$ is the relative frequency of pure Type I conduction channels in the MOF film. $\sigma_{\mathrm{nanocrystal}}^{\mathrm{Type\ I}}$ is the conductivity of a single Type I nanocrystal, which has the same value as $\sigma_{\mathrm{channel}}^{\mathrm{pure\ Type\ I}}$. Thus, the MOF film conductivity can be approximated by the Mg²⁺ conductivity of a Type I nanocrystal, scaled by the relative frequency of the pure Type I conduction channel.

Based on this analysis, we used the temperature-dependent Mg^{2+} conductivity of the Type I nanocrystal (red curve in Figure 7d) to predict the apparent activation energy (E_a) for Mg^{2+} conduction in the MOF film (Figure 7e). We obtained E_a by fitting the logarithm of conductivity to the inverse temperature. Importantly, because E_a corresponds to the slope of the fit curve, it is independent of any assumptions regarding the relative frequency of the pure Type I conduction channel. That is to say, the prediction of E_a does not rely on empirical input. We calculated E_a for Mg^{2+} conduction in the MOF film to be 5.45 kcal/mol (Figure 7d). At the same time, we measured the temperature-dependent Mg^{2+} conductivity of the MOF thin film to determine the experimental apparent activation energy (Figure 7e). The experimental value for E_a was found to be 5.16 kcal/mol, which is in good agreement with the predicted value. This serves to validate the results of our interface calculations and kinetic modeling approach. E_a for Mg^{2+} conduction in the MOF-74 film is slightly larger than that

measured by Aubrey et al. for the MOF-pressed pellet (2.5–4.4 kcal/mol, depending on electrolyte composition). This might be attributed to the presence of electrolyte-filled gaps in the pellet, which can enhance ion conduction.

In addition, we note that Mg²⁺ conductivities of the Type I nanocrystal (red curve in Figure 7d) are approximately 2-3 orders of magnitude greater than the experimentally measured conductivities of the MOF film (Figure 7f), for all temperature values. This discrepancy can be precisely accounted for by eq 16, where the film conductivity is equal to the Type I nanocrystal conductivity scaled by some factor $\left(\frac{N_{\text{pure Type I}}}{N}\right)$. This factor corresponds to the relative frequency of pure Type I conduction channels in the MOF film and is independent of temperature. Comparing Type I nanocrystal conductivities with experimental film conductivities, we find that a scaling factor of 0.2% best accounts for the experimental data. This implies that the relative frequency of pure Type I conduction channels in the experimental MOF film is around 0.2%. Applying this factor, the final predicted Mg²⁺ conductivity of the MOF film (Figure 7e) agrees closely with the experimentally measured conductivity (Figure 7f) at all temperatures, including room temperature ($\sigma_{300\text{K}}$). In this way, our approach can combine theoretical calculations with experimental measurements to characterize the interface composition of MOF.

Together, these results indicate that Mg²⁺ transport in the MOF-74 thin film occurs primarily through conduction channels composed of only nanocrystals with aligned interfaces (i.e., Type I-like interfaces). This is because the presence of any misaligned interfaces (i.e., Type II/III-like interfaces) greatly decreases the rate of Mg²⁺ transport through the conduction channel. Moreover, the relative frequency of perfectly aligned (i.e., pure Type I) conduction channels in the MOF film is exceedingly small (approximately 0.2%). This is consistent with a disordered arrangement of nanocrystals and grain boundaries. The small number of fully aligned channels, through which Mg²⁺ transport overwhelmingly occurs, leads to a 2-3 order-ofmagnitude decrease in the ion conductivity of the MOF thin film. These insights into the physical composition and transport properties of MOF-74 are validated by the accurate prediction of apparent activation energy (Figure 7e,f). In addition, the relatively large capacitances measured for the MOF-74 thin film (20-60 nF; refer to Table S5) suggest strong effects from the electrical double layer at grain boundaries, consistent with the important role of grain boundary ion transport. 76

To further discuss the parameters used in the MOF nanocrystal model, we emphasize that the scaling factor $\left(\frac{N_{\text{pure Type1}}}{N}\right)$ in eq 16 is the only parameter obtained through empirical fitting. It corresponds to the frequency with which aligned MOF grain boundaries occur. Although the conductivity prediction is partly determined by this parameter, predicted E_{a} is independent of $\frac{N_{\text{pure Type1}}}{N}$ and does not rely on empirical input. E_{a} is the key quantity for governing ion transport kinetics and can be used to screen solid-state conductors. On the other hand, determining the value of $\frac{N_{\text{pure Type1}}}{N}$, through combining theoretical calculations with experimental measurements, represents a quantitative characterization of the grain boundary composition of the MOF-74 film, which is further explored in Section 4.5.5.

In addition, we note that the comparison between predicted and experimental ion conductivities does not account for the

effect of anion (TFSI⁻) transport. However, based on our calculations, the transport barrier for TFSI is significantly elevated due to OMS binding (30 kcal/mol at the PBE-D2 level; Figure S18) and much higher than that for Mg²⁺ conduction (5.9 kcal/mol; Figure 3). Because of this, we expect only a small contribution from anion transport to total conductivity, with the transference number of Mg²⁺ close to unity.

As a final point, a potential source of error in the ion conductivity measurement can arise from ion correlation effects at low temperatures.⁷⁷ This is hinted at by depressed semicircles in the corresponding Nyquist plots (Figure S9d). Correlated ion dynamics are not accounted for in the current modeling approach, and the temperatures at which they become relevant for Mg-MOF-74 are less certain. Accordingly, the presence of correlated ion conduction in the MOF-74 system merits further investigation, though it is beyond the scope of the present work.

4.5.5. Characterizing Grain Boundary Composition. To better understand the composition of the MOF grain boundary and its role in modulating ion conductivity, we conceive the MOF film as composed of parallel ion conduction channels (Figure S17a). Although this is a simplified assumption, we use it as a first-order approximation. Given the thickness of the MOF film (~200 nm), each conduction channel contains around six MOF nanocrystals. The interfaces separating adjacent nanocrystals in the conduction channel can be either Type I-like (aligned) or Type II/III-like (misaligned). The frequency with which a given interface occurs in MOF is determined by the formation probability of that interface type.

If the formation of MOF grain boundaries is determined by thermodynamics, then the formation probabilities of different interface types obey the Boltzmann distribution. Because the Type I interface is more stable than Type II and III interfaces by $8-10 \text{ kcal mol}^{-1} \text{ Å}^{-2}$ (refer to Section 4.2.3), this would lead to a formation probability of >99% for Type I-like interfaces. That is to say, the overwhelming majority of MOF grain boundaries would be highly aligned. In this case, the distribution of ion conduction channels significantly favors (>90% relative frequency) channels containing only Type I-like interfaces (Figure S17b, blue distribution). The resulting Mg²⁺ conductivity of the MOF film is 2-3 orders of magnitude greater than the experimental conductivity, although the apparent activation energy is still similar (Figure S17c, blue plot).

On the other hand, if MOF grain boundary formation is primarily controlled by the kinetics of the formation process, then the formation probabilities can differ from the Boltzmann distribution. If formation kinetics is the same for all interfaces, then the formation probabilities of Type I, II, and III interfaces, given their geometries, would also be the same (i.e., 33% for each). In this case, the distribution of ion conduction channels favors mainly mixed channels and channels in which Type II/IIIlike (misaligned) interfaces dominate (Figure S17b, red distribution). The relative frequency of the pure Type I channel is 0.1%, close to the empirically fitted value (0.2%). The MOF film conductivity and apparent activation energy are also close to the experiment (Figure S17c, red plot). Finally, we note that a formation probability of around 36% for Type I-like interfaces gives exactly 0.2% relative frequency for pure Type I conduction channels (Figure S17b, gray distribution), as well as the best agreement with experiment in terms of conductivity (Figure \$17c, gray plot).

Our analysis shows that a largely random formation process for MOF grain boundaries, where the formation probabilities of all interfaces are almost the same, produces fully aligned ion

conduction channels at a frequency of 0.1–0.2%, corresponding to the empirically determined value. This result is consistent with the disordered arrangement of MOF nanocrystals. It also suggests that grain boundary composition in MOF-74 is kinetically controlled rather than depending on the thermodynamic stabilities of interfaces.

5. CONCLUSIONS

Combining computational and experimental methods, we have developed and validated an approach for investigating grain boundary effects on ion transport in MOF-based solid-state materials. In particular, we focused on Mg²⁺ conduction in the Mg-MOF-74 thin film as a representative system. With XRD analysis, we determined the relative orientation and grain size of MOF-74 nanocrystals. The molecular-level properties of the MOF nanocrystal surface and surface-surface interfaces were then studied by DFT. Energy barriers for Mg²⁺ transport in the nanocrystal interior and at the grain boundary were computed. Using these results, we developed an ion transport model of the MOF nanocrystal, incorporating both bulk structure and grain boundaries. This model was used to predict the temperaturedependent Mg²⁺ conductivity of the Mg-MOF-74 thin film. The predicted apparent activation energy (5.45 kcal/mol) and conductivity ($\sim 10^{-6}$ S/cm) agree well with experimentally measured values (5.16 kcal/mol and 1.62×10^{-6} S/cm), which validates our methods. Finally, our model was applied to characterize the grain boundary composition of MOF-74.

Our results indicate that Mg²⁺ transport in MOF-74 is significantly hindered by grain boundaries. Physically, this is due to strong Mg²⁺ interactions with the MOF linker, which partly traps Mg²⁺ at the grain boundary interface. Escaping from these interfacial interactions requires overcoming relatively large energy barriers. On the other hand, interfaces with highly aligned MOF pores allow for Mg²⁺ transport without the formation of interfacial interactions, similar to bulk MOF. Accordingly, MOF nanocrystals with aligned grain boundaries exhibit ion conductivities multiple orders of magnitude higher than misaligned nanocrystals. Moreover, Mg²⁺ transport in MOF occurs overwhelmingly through ion conduction channels with aligned grain boundaries. However, the low frequency (0.1–0.2%) with which fully aligned channels occur limits ion conductivity. This low frequency suggests that MOF nanocrystal arrangement is disordered, with their grain boundary composition controlled by the kinetics of the formation process.

These conclusions suggest potential strategies for overcoming limitations to MOF-74 ion conductivity. One approach is to reduce the frequency of misaligned grain boundaries, either by increasing grain size or through orientation control. An alternative would be to prevent the formation of strong ionlinker interactions at the grain boundary interface. This can be achieved through modification of the MOF linker or functionalization of the nanocrystal surface.

The current work demonstrates the important role of grain boundaries in controlling MOF-74 ion conduction and elucidates the physical mechanisms by which this occurs. By combining theory and experiment, it can be further extended for conductivity prediction and grain boundary characterization in a wide range of MOF-based ion conductors.

ASSOCIATED CONTENT

Supporting Information

The Supporting Information is available free of charge at https://pubs.acs.org/doi/10.1021/acsami.3c02329.

Optimized supercell of Mg-MOF-74; models used to study Mg²⁺ transport at Type I, II, and III interfaces; models used to study Mg²⁺ transport at Type IV and V interfaces; carved cluster models of bulk MOF and Type I-IV interfaces; comparison of Mg²⁺ solvation for the SCCS model and PCM; atom subsets used to estimate vibrational free energies; convergence of Mg²⁺ concentration in the nanocrystal kinetic model; XRD patterns of the Mg-MOF-74 thin film and powder; measuring ion conductivity in Mg-MOF-74; H₂O binding to unsaturated metal nodes at the MOF nanocrystal surface; MEP and energy barriers for DME solvent displacement; models used to study hopping distances and interface alignments; MEP and energy barriers with different hopping distances; MEP and energy barriers with different interface alignments; bulk, interface, and combined conductivities of MOF nanocrystals; alternate MOF nanocrystal kinetic model with a symmetric interface; analysis of ion conduction channels in the MOF-74 thin film; MEP and energy barrier for TFSI⁻ transport; temperature-dependent free energy barriers and rate constants for bulk MOF; temperature-dependent free energy barriers and rate constants for the Type I interface; temperature-dependent free energy barriers and rate constants for the Type II interface; temperaturedependent free energy barriers and rate constants for the Type III interface; fitted parameters for an equivalent circuit; grain size of the Mg-MOF-74 nanocrystal estimated by XRD; sample input file for structure relaxation of the o-surface; sample input file for CI-NEB calculation on the Type I interface; sample input file for single-point calculation on the Type I interface carved cluster; sample input file for SCCS calculation on the Type I interface; sample input file for SMD calculation on the Type I interface carved cluster; sample input file for PCM calculation on the Type I interface carved cluster; sample input file for KMC simulations with the nanocrystal kinetic model; sample input file for KMC simulations with the alternate kinetic model (PDF)

AUTHOR INFORMATION

Corresponding Authors

Dunwei Wang - Department of Chemistry, Boston College, Chestnut Hill, Massachusetts 02467, United States; orcid.org/0000-0001-5581-8799; Email: dunwei.wang@

Udayan Mohanty - Department of Chemistry, Boston College, Chestnut Hill, Massachusetts 02467, United States;

orcid.org/0000-0002-8778-974X; Email: mohanty@ bc.edu

Junwei Lucas Bao – Department of Chemistry, Boston College, Chestnut Hill, Massachusetts 02467, United States; orcid.org/0000-0002-4967-663X; Email: lucas.bao@

bc.edu **Authors**

Yang Wang - Department of Chemistry, Boston College, Chestnut Hill, Massachusetts 02467, United States Tongtong Luo – Department of Chemistry, Boston College, Chestnut Hill, Massachusetts 02467, United States Brooke Elander - Department of Chemistry, Boston College, Chestnut Hill, Massachusetts 02467, United States; orcid.org/0000-0002-6649-474X

Yu Mu - Department of Chemistry, Boston College, Chestnut Hill, Massachusetts 02467, United States

Complete contact information is available at: https://pubs.acs.org/10.1021/acsami.3c02329

Author Contributions

[‡]Y.W. and T.L. contributed equally to this work. All authors contributed to manuscript preparation.

Notes

The authors declare no competing financial interest.

ACKNOWLEDGMENTS

D.W., U.M., and J.L.B. acknowledge the support of the National Science Foundation under Grant DMR-2126923. T.L. and D.W. are grateful to a RAD grant from Boston College. The authors thank the Boston College Linux cluster for computational resources.

REFERENCES

- (1) Zhang, Z.; Shao, Y.; Lotsch, B.; Hu, Y.-S.; Li, H.; Janek, J.; F Nazar, L.; Nan, C.-W.; Maier, J.; Armand, M.; Chen, L. New Horizons for Inorganic Solid State Ion Conductors. Energy Environ. Sci. 2018, 11, 1945-1976.
- (2) Furukawa, H.; Cordova, K. E.; O'Keeffe, M.; Yaghi, O. M. The Chemistry and Applications of Metal-Organic Frameworks. Science 2013, 341, No. 1230444.
- (3) Rosi, N. L.; Kim, J.; Eddaoudi, M.; Chen, B.; O'Keeffe, M.; Yaghi, O. M. Rod Packings and Metal-Organic Frameworks Constructed from Rod-Shaped Secondary Building Units. J. Am. Chem. Soc. 2005, 127, 1504-1518.
- (4) Wiers, B. M.; Foo, M.-L.; Balsara, N. P.; Long, J. R. A Solid Lithium Electrolyte via Addition of Lithium Isopropoxide to a Metal-Organic Framework with Open Metal Sites. J. Am. Chem. Soc. 2011, 133, 14522-14525.
- (5) Miner, E. M.; Park, S. S.; Dincă, M. High Li⁺ and Mg²⁺ Conductivity in a Cu-Azolate Metal-Organic Framework. J. Am. Chem. Soc. 2019, 141, 4422-4427.
- (6) Aubrey, M. L.; Ameloot, R.; Wiers, B. M.; Long, J. R. Metal-Organic Frameworks as Solid Magnesium Electrolytes. Energy Environ. Sci. **2014**, 7, 667–671.
- (7) Yuan, S.; Bao, J. L.; Wei, J.; Xia, Y.; Truhlar, D. G.; Wang, Y. A Versatile Single-Ion Electrolyte with a Grotthuss-like Li Conduction Mechanism for Dendrite-Free Li Metal Batteries. Energy Environ. Sci. **2019**, *12*, 2741–2750.
- (8) Park, S. S.; Tulchinsky, Y.; Dincă, M. Single-Ion Li⁺, Na⁺, and Mg²⁺ Solid Electrolytes Supported by a Mesoporous Anionic Cu-Azolate Metal-Organic Framework. J. Am. Chem. Soc. 2017, 139, 13260-
- (9) Shen, L.; Wu, H. B.; Liu, F.; Brosmer, J. L.; Shen, G.; Wang, X.; Zink, J. I.; Xiao, Q.; Cai, M.; Wang, G.; Lu, Y.; Dunn, B. Creating Lithium-Ion Electrolytes with Biomimetic Ionic Channels in Metal-Organic Frameworks. Adv. Mater. 2018, 30, No. 1707476.
- (10) Xu, W.; Pei, X.; Diercks, C. S.; Lyu, H.; Ji, Z.; Yaghi, O. M. A Metal-Organic Framework of Organic Vertices and Polyoxometalate Linkers as a Solid-State Electrolyte. J. Am. Chem. Soc. 2019, 141, 17522-17526.
- (11) He, Y.; Qiao, Y.; Chang, Z.; Zhou, H. The Potential of Electrolyte Filled MOF Membranes as Ionic Sieves in Rechargeable Batteries. Energy Environ. Sci. 2019, 12, 2327-2344.
- (12) Liu, L.; Sun, C. Flexible Quasi-Solid-State Composite Electrolyte Membrane Derived from a Metal-Organic Framework for Lithium-Metal Batteries. ChemElectroChem 2020, 7, 707-715.
- (13) Shen, L.; Wu, H. B.; Liu, F.; Zhang, C.; Ma, S.; Le, Z.; Lu, Y. Anchoring Anions with Metal-Organic Framework-Functionalized Separators for Advanced Lithium Batteries. Nanoscale Horiz. 2019, 4, 705 - 711.

- (14) Tang, A.; He, X.; Yin, H.; Li, Y.; Zhang, Y.; Huang, S.; Truhlar, D. G. UiO-66 Metal—Organic Framework as an Anode for a Potassium-Ion Battery: Quantum Mechanical Analysis. *J. Phys. Chem. C* **2021**, *125*, 9679—9687.
- (15) Wei, Y.; Tang, A.; He, X.; Chen, H.; Yin, H.; Li, Y.; Zhang, Y.; Huang, S. Potassium Storage Performance of UiO-66 Derivatives from First Principles Calculations. *J. Phys. Chem. C* **2022**, *126*, 4286–4295.
- (16) Li, M.; Wan, Y.; Huang, J.-K.; Assen, A. H.; Hsiung, C.-E.; Jiang, H.; Han, Y.; Eddaoudi, M.; Lai, Z.; Ming, J.; Li, L.-J. Metal—Organic Framework-Based Separators for Enhancing Li—S Battery Stability: Mechanism of Mitigating Polysulfide Diffusion. *ACS Energy Lett.* **2017**, 2, 2362–2367.
- (17) Luo, J.; Li, Y.; Zhang, H.; Wang, A.; Lo, W.-S.; Dong, Q.; Wong, N.; Povinelli, C.; Shao, Y.; Chereddy, S.; Wunder, S.; Mohanty, U.; Tsung, C.-K.; Wang, D. A Metal—Organic Framework Thin Film for Selective Mg²⁺ Transport. *Angew. Chem., Int. Ed.* **2019**, *58*, 15313—15317.
- (18) Mei, A.; Wang, X.-L.; Lan, J.-L.; Feng, Y.-C.; Geng, H.-X.; Lin, Y.-H.; Nan, C.-W. Role of Amorphous Boundary Layer in Enhancing Ionic Conductivity of Lithium—Lanthanum—Titanate Electrolyte. *Electrochim. Acta* **2010**, *55*, 2958—2963.
- (19) Ma, C.; Chen, K.; Liang, C.; Nan, C.-W.; Ishikawa, R.; More, K.; Chi, M. Atomic-Scale Origin of the Large Grain-Boundary Resistance in Perovskite Li-Ion-Conducting Solid Electrolytes. *Energy Environ. Sci.* **2014**, *7*, 1638–1642.
- (20) Dawson, J. A.; Canepa, P.; Famprikis, T.; Masquelier, C.; Islam, M. S. Atomic-Scale Influence of Grain Boundaries on Li-Ion Conduction in Solid Electrolytes for All-Solid-State Batteries. *J. Am. Chem. Soc.* **2018**, *140*, 362–368.
- (21) Sasano, S.; Ishikawa, R.; Kawahara, K.; Kimura, T.; Ikuhara, Y. H.; Shibata, N.; Ikuhara, Y. Grain Boundary Li-Ion Conductivity in (Li_{0.33}La_{0.56})TiO₃ Polycrystal. *Appl. Phys. Lett.* **2020**, *116*, No. 043901.
- (22) Shen, K.; Wang, Y.; Zhang, J.; Zong, Y.; Li, G.; Zhao, C.; Chen, H. Revealing the Effect of Grain Boundary Segregation on Li Ion Transport in Polycrystalline Anti-Perovskite Li₃ClO: A Phase Field Study. *Phys. Chem. Chem. Phys.* **2020**, 22, 3030–3036.
- (23) Bogusz, W.; Krok, F.; Jakubowski, W. Bulk and Grain Boundary Electrical Conductivities of NASICON. *Solid State Ionics* **1981**, 2, 171–174
- (24) Lunghammer, S.; Ma, Q.; Rettenwander, D.; Hanzu, I.; Tietz, F.; Wilkening, H. M. R. Bulk and Grain-Boundary Ionic Conductivity in Sodium Zirconophosphosilicate Na₃Zr₂(SiO₄)₂PO₄ (NASICON). *Chem. Phys. Lett.* **2018**, 701, 147–150.
- (25) Martin, M. C.; Mecartney, M. L. Grain Boundary Ionic Conductivity of Yttrium Stabilized Zirconia as a Function of Silica Content and Grain Size. *Solid State Ionics* **2003**, *161*, 67–79.
- (26) Moriwake, H.; Kuwabara, A.; Fisher, C. A. J.; Huang, R.; Hitosugi, T.; Ikuhara, Y. H.; Oki, H.; Ikuhara, Y. First-Principles Calculations of Lithium-Ion Migration at a Coherent Grain Boundary in a Cathode Material, LiCoO₂. Adv. Mater. **2013**, 25, 618–622.
- (27) Gregori, G.; Merkle, R.; Maier, J. Ion Conduction and Redistribution at Grain Boundaries in Oxide Systems. *Prog. Mater. Sci.* **2017**, *89*, 252–305.
- (28) Shiiba, H.; Zettsu, N.; Yamashita, M.; Onodera, H.; Jalem, R.; Nakayama, M.; Teshima, K. Molecular Dynamics Studies on the Lithium Ion Conduction Behaviors Depending on Tilted Grain Boundaries with Various Symmetries in Garnet-Type Li₇La₃Zr₂O₁₂. *J. Phys. Chem. C* **2018**, *122*, 21755–21762.
- (29) Kuhn, A.; Narayanan, S.; Spencer, L.; Goward, G.; Thangadurai, V.; Wilkening, M. Li Self-Diffusion in Garnet-Type Li₇La₃Zr₂O₁₂ as Probed Directly by Diffusion-Induced ⁷Li Spin-Lattice Relaxation NMR Spectroscopy. *Phys. Rev. B* **2011**, *83*, No. 094302.
- (30) Huang, S.; Wilson, B. E.; Wang, B.; Fang, Y.; Buffington, K.; Stein, A.; Truhlar, D. G. Y-Doped Li₈ZrO₆: A Li-Ion Battery Cathode Material with High Capacity. *J. Am. Chem. Soc.* **2015**, *137*, 10992–11003.
- (31) Shen, K.; He, R.; Wang, Y.; Zhao, C.; Chen, H. Atomistic Insights into the Role of Grain Boundary in Ionic Conductivity of Polycrystalline Solid-State Electrolytes. *J. Phys. Chem. C* **2020**, *124*, 26241–26248.

- (32) Øien, S.; Wragg, D.; Reinsch, H.; Svelle, S.; Bordiga, S.; Lamberti, C.; Lillerud, K. P. Detailed Structure Analysis of Atomic Positions and Defects in Zirconium Metal—Organic Frameworks. *Cryst. Growth Des.* **2014**, *14*, 5370–5372.
- (33) Zhu, Y.; Zheng, J.; Ye, J.; Cui, Y.; Koh, K.; Kovarik, L.; Camaioni, D. M.; Fulton, J. L.; Truhlar, D. G.; Neurock, M.; Cramer, C. J.; Gutiérrez, O. Y.; Lercher, J. A. Copper-Zirconia Interfaces in UiO-66 Enable Selective Catalytic Hydrogenation of CO₂ to Methanol. *Nat. Commun.* **2020**, *11*, No. 5849.
- (34) Ye, J.; Neurock, M.; Truhlar, D. G. Effect of Missing-Linker Defects on CO₂ Hydrogenation to Methanol by Cu Nanoparticles in UiO-66. *J. Phys. Chem. C* **2022**, *126*, 13157–13167.
- (35) Levenson, D. A.; Zhang, J.; S Gelfand, B.; P Kammampata, S.; Thangadurai, V.; H Shimizu, G. K. Particle Size Dependence of Proton Conduction in a Cationic Lanthanum Phosphonate MOF. *Dalton Trans.* **2020**, *49*, 4022–4029.
- (36) Sun, Y.; Song, C.; Guo, X.; Liu, Y. Concurrent Manipulation of Out-of-Plane and Regional In-Plane Orientations of NH₂-UiO-66 Membranes with Significantly Reduced Anisotropic Grain Boundary and Superior $\rm H_2/CO_2$ Separation Performance. ACS Appl. Mater. Interfaces 2020, 12, 4494–4500.
- (37) Zheng, R.; Fu, Z.-H.; Deng, W.-H.; Wen, Y.; Wu, A.-Q.; Ye, X.-L.; Xu, G. The Growth Mechanism of a Conductive MOF Thin Film in Spray-Based Layer-by-Layer Liquid Phase Epitaxy. *Angew. Chem., Int. Ed.* **2022**, *61*, No. e202212797.
- (38) Hou, Q.; Zhou, S.; Wei, Y.; Caro, J.; Wang, H. Balancing the Grain Boundary Structure and the Framework Flexibility through Bimetallic Metal—Organic Framework (MOF) Membranes for Gas Separation. J. Am. Chem. Soc. 2020, 142, 9582—9586.
- (39) Dzubak, A. L.; Lin, L.-C.; Kim, J.; Swisher, J. A.; Poloni, R.; Maximoff, S. N.; Smit, B.; Gagliardi, L. *Ab Initio* Carbon Capture in Open-Site Metal—Organic Frameworks. *Nat. Chem.* **2012**, *4*, 810–816.
- (40) Lee, K.; Howe, J. D.; Lin, L.-C.; Smit, B.; Neaton, J. B. Small-Molecule Adsorption in Open-Site Metal—Organic Frameworks: A Systematic Density Functional Theory Study for Rational Design. *Chem. Mater.* **2015**, *27*, 668–678.
- (41) Canepa, P.; Nijem, N.; Chabal, Y. J.; Thonhauser, T. Diffusion of Small Molecules in Metal Organic Framework Materials. *Phys. Rev. Lett.* **2013**, *110*, No. 026102.
- (42) Vlaisavljevich, B.; Huck, J.; Hulvey, Z.; Lee, K.; Mason, J. A.; Neaton, J. B.; Long, J. R.; Brown, C. M.; Alfè, D.; Michaelides, A.; Smit, B. Performance of van Der Waals Corrected Functionals for Guest Adsorption in the $M_2(Dobdc)$ Metal—Organic Frameworks. J. Phys. Chem. A 2017, 121, 4139—4151.
- (43) de Oliveira, A.; de Lima, G. F.; De Abreu, H. A. Structural and Electronic Properties of M-MOF-74 (M = Mg, Co or Mn). *Chem. Phys. Lett.* **2018**, *691*, 283–290.
- (44) Yoo, H. D.; Shterenberg, I.; Gofer, Y.; Gershinsky, G.; Pour, N.; Aurbach, D. Mg Rechargeable Batteries: An On-Going Challenge. *Energy Environ. Sci.* **2013**, *6*, 2265–2279.
- (45) Yang, S.; Li, D.; Zhang, T.; Tao, Z.; Chen, J. First-Principles Study of Zigzag MoS₂ Nanoribbon As a Promising Cathode Material for Rechargeable Mg Batteries. *J. Phys. Chem. C* **2012**, *116*, 1307–1312.
- (46) Nakano, K.; Noda, Y.; Tanibata, N.; Nakayama, M.; Kajihara, K.; Kanamura, K. Computational Investigation of the Mg-Ion Conductivity and Phase Stability of MgZr₄(PO₄)₆. RSC Adv. **2019**, *9*, 12590–12595.
- (47) Song, J.; Sahadeo, E.; Noked, M.; Lee, S. B. Mapping the Challenges of Magnesium Battery. *J. Phys. Chem. Lett.* **2016**, *7*, 1736–1749.
- (48) Wang, Y.; Luo, T.; Li, Y.; Wang, A.; Wang, D.; Bao, J. L.; Mohanty, U.; Tsung, C.-K. Molecular-Level Insights into Selective Transport of Mg²⁺ in Metal—Organic Frameworks. *ACS Appl. Mater. Interfaces* **2021**, *13*, 51974—51987.
- (49) Giannozzi, P.; Baroni, S.; Bonini, N.; Calandra, M.; Car, R.; Cavazzoni, C.; Ceresoli, D.; Chiarotti, G. L.; Cococcioni, M.; Dabo, I.; Corso, A. D.; Gironcoli, S.; de Fabris, S.; Fratesi, G.; Gebauer, R.; Gerstmann, U.; Gougoussis, C.; Kokalj, A.; Lazzeri, M.; Martin-Samos, L.; Marzari, N.; Mauri, F.; Mazzarello, R.; Paolini, S.; Pasquarello, A.; Paulatto, L.; Sbraccia, C.; Scandolo, S.; Sclauzero, G.; Seitsonen, A. P.;

- Smogunov, A.; Umari, P.; Wentzcovitch, R. M. QUANTUM ESPRESSO: A Modular and Open-Source Software Project for Quantum Simulations of Materials. J. Phys.: Condens. Matter 2009, 21, No. 395502.
- (50) Perdew, J. P.; Burke, K.; Ernzerhof, M. Generalized Gradient Approximation Made Simple. Phys. Rev. Lett. 1996, 77, 3865-3868.
- (51) Grimme, S. Semiempirical GGA-type density functional constructed with a long-range dispersion correction. J. Comput. Chem. 2006, 27, 1787-1799.
- (52) Vanderbilt, D. Soft Self-Consistent Pseudopotentials in a Generalized Eigenvalue Formalism. Phys. Rev. B 1990, 41, 7892-7895.
- (53) Henkelman, G.; Uberuaga, B. P.; Jónsson, H. A Climbing Image Nudged Elastic Band Method for Finding Saddle Points and Minimum Energy Paths. J. Chem. Phys. 2000, 113, 9901-9904.
- (54) Zhao, Y.; Truhlar, D. G. The M06 Suite of Density Functionals for Main Group Thermochemistry, Thermochemical Kinetics, Noncovalent Interactions, Excited States, and Transition Elements: Two New Functionals and Systematic Testing of Four M06-Class Functionals and 12 Other Functionals. Theor. Chem. Acc. 2008, 120, 215-
- (55) Zhao, Y.; Truhlar, D. G. Density Functionals with Broad Applicability in Chemistry. Acc. Chem. Res. 2008, 41, 157–167.
- (56) Zheng, J.; Zhao, Y.; Truhlar, D. G. The DBH24/08 Database and Its Use to Assess Electronic Structure Model Chemistries for Chemical Reaction Barrier Heights. J. Chem. Theory Comput. 2009, 5, 808-821.
- (57) Frisch, M. J.; Trucks, G. W.; Schlegel, H. B.; Scuseria, G. E.; Robb, M. A.; Cheeseman, J. R.; Scalmani, G.; Barone, V.; Petersson, G. A.; Nakatsuji, H.; Li, X.; Caricato, M.; Marenich, A. V.; Bloino, J.; Janesko, B. G.; Gomperts, R.; Mennucci, B.; Hratchian, H. P.; Ortiz, J. V.; Izmaylov, A. F.; Sonnenberg, J. L.; Williams; Ding, F.; Lipparini, F.; Egidi, F.; Goings, J.; Peng, B.; Petrone, A.; Henderson, T.; Ranasinghe, D.; Zakrzewski, V. G.; Gao, J.; Rega, N.; Zheng, G.; Liang, W.; Hada, M.; Ehara, M.; Toyota, K.; Fukuda, R.; Hasegawa, J.; Ishida, M.; Nakajima, T.; Honda, Y.; Kitao, O.; Nakai, H.; Vreven, T.; Throssell, K.; Montgomery, J. A., Jr.; Peralta, J. E.; Ogliaro, F.; Bearpark, M. J.; Heyd, J. J.; Brothers, E. N.; Kudin, K. N.; Staroverov, V. N.; Keith, T. A.; Kobayashi, R.; Normand, J.; Raghavachari, K.; Rendell, A. P.; Burant, J. C.; Iyengar, S. S.; Tomasi, J.; Cossi, M.; Millam, J. M.; Klene, M.; Adamo, C.; Cammi, R.; Ochterski, J. W.; Martin, R. L.; Morokuma, K.; Farkas, O.; Foresman, J. B.; Fox, D. J. Gaussian 16 Rev. C.01, 2016.
- (58) Andreussi, O.; Dabo, I.; Marzari, N. Revised Self-Consistent Continuum Solvation in Electronic-Structure Calculations. J. Chem. Phys. 2012, 136, No. 064102.
- (59) Marenich, A. V.; Cramer, C. J.; Truhlar, D. G. Universal Solvation Model Based on Solute Electron Density and on a Continuum Model of the Solvent Defined by the Bulk Dielectric Constant and Atomic Surface Tensions. J. Phys. Chem. B 2009, 113, 6378-6396.
- (60) Tomasi, J.; Mennucci, B.; Cammi, R. Quantum Mechanical Continuum Solvation Models. Chem. Rev. 2005, 105, 2999-3094.
- (61) Dupont, C.; Andreussi, O.; Marzari, N. Self-Consistent Continuum Solvation (SCCS): The Case of Charged Systems. J. Chem. Phys. 2013, 139, No. 214110.
- (62) Togo, A.; Tanaka, I. First Principles Phonon Calculations in Materials Science. Scr. Mater. 2015, 108, 1-5.
- (63) Bao, J. L.; Truhlar, D. G. Variational Transition State Theory: Theoretical Framework and Recent Developments. Chem. Soc. Rev. **2017**, *46*, 7548–7596.
- (64) Kramers, H. A. Brownian Motion in a Field of Force and the Diffusion Model of Chemical Reactions. Physica 1940, 7, 284-304.
- (65) Grote, R. F.; Van der Zwan, G.; Hynes, J. T. Frequency-Dependent Friction and Solution Reaction Rates. J. Phys. Chem. A 1984, 88, 4676-4684.
- (66) Grote, R. F.; Hynes, J. T. The Stable States Picture of Chemical Reactions. II. Rate Constants for Condensed and Gas Phase Reaction Models. J. Chem. Phys. 1980, 73, 2715-2732.
- (67) Ling, C.; Suto, K. Thermodynamic Origin of Irreversible Magnesium Trapping in Chevrel Phase Mo6S8: Importance of Magnesium and Vacancy Ordering. Chem. Mater. 2017, 29, 3731-3739.

- (68) He, X.; Zhu, Y.; Epstein, A.; Mo, Y. Statistical Variances of Diffusional Properties from Ab Initio Molecular Dynamics Simulations. npj Comput. Mater. 2018, 4, No. 18.
- (69) Gillespie, D. T. A General Method for Numerically Simulating the Stochastic Time Evolution of Coupled Chemical Reactions. J. Comput. Phys. 1976, 22, 403-434.
- (70) Sanft, K. R.; Wu, S.; Roh, M.; Fu, J.; Lim, R. K.; Petzold, L. R. StochKit2: Software for Discrete Stochastic Simulation of Biochemical Systems with Events. Bioinformatics 2011, 27, 2457-2458
- (71) Abel, J. H.; Drawert, B.; Hellander, A.; Petzold, L. R. GillesPy: A Python Package for Stochastic Model Building and Simulation. IEEE Life Sci. Lett. 2016, 2, 35-38.
- (72) Patterson, A. L. The Scherrer Formula for X-Ray Particle Size Determination. Phys. Rev. 1939, 56, 978-982.
- (73) Yao, X.; Luo, J.; Dong, Q.; Wang, D. A Rechargeable Non-Aqueous Mg-Br₂ Battery. Nano Energy 2016, 28, 440-446.
- (74) Gao, T.; Hou, S.; Wang, F.; Ma, Z.; Li, X.; Xu, K.; Wang, C. Reversible S^0/MgS_x Redox Chemistry in a $MgTFSI_2/MgCl_2/DME$ Electrolyte for Rechargeable Mg/S Batteries. Angew. Chem. 2017, 129, 13711-13715.
- (75) Onuchic, J. N.; Beratan, D. N.; Winkler, J. R.; Gray, H. B. Pathway Analysis of Protein Electron-Transfer Reactions. Annu. Rev. Biophys. Biomol. Struct. 1992, 21, 349-377.
- (76) Irvine, J. T. S.; Sinclair, D. C.; West, A. R. Electroceramics: Characterization by Impedance Spectroscopy. Adv. Mater. 1990, 2,
- (77) Zettl, R.; Lunghammer, S.; Gadermaier, B.; Boulaoued, A.; Johansson, P.; Wilkening, H. M. R.; Hanzu, I. High Li+ and Na+ Conductivity in New Hybrid Solid Electrolytes Based on the Porous MIL-121 Metal Organic Framework. Adv. Energy Mater. 2021, 11, No. 2003542.

□ Recommended by ACS

First-Principles Study of 2D Haeckelite C₇N as a High-**Capacity Anode for Post-Lithium-Ion Batteries**

Zahra Hajiahmadi, S. Shahab Naghavi, et al.

II II Y 07 2023

ACS APPLIED NANO MATERIALS

READ 2

Structural Transformations at the Atomic Scale in Spinel Vanadium Oxides upon Mg2+ Extraction

Francisco Lagunas, Robert F. Klie, et al.

MAY 16, 2023

ACS APPLIED ENERGY MATERIALS

READ **C**

Ionic Dynamics of the Charge Carrier in Layered Solid Materials for Mg Rechargeable Batteries

Chuhong Wang, Rajeev S. Assary, et al.

SEPTEMBER 22, 2022

CHEMISTRY OF MATERIALS

READ **C**

Coordination-Dependent Chemical Reactivity of TFSI Anions at a Mg Metal Interface

Venkateshkumar Prabhakaran, Vijayakumar Murugesan, et al.

JANUARY 30, 2023

ACS APPLIED MATERIALS & INTERFACES

READ 2

Get More Suggestions >